HELLENIC REPUBLIC
National and Kapodistrian University of Athens
EST. 1837

School of Health Sciences

School of Medicine and Department of Pharmacy

Interdisciplinary M.Sc course in

Nanomedicine

Academic year 2019-2020

"Development of novel conjugated polymer nanoparticles for photoacoustic bioimaging"

Mavronasou Aikaterini Maria

Supervisor: Associate Prof. Dionysios E. Mouzakis

Co-supervisor: Dr. Christos Chochos, NHRF, Institute of Chemical Biology

Committee Members: Professor Hermis Iatrou

Associate researcher Nefeli Lagopati

ATHENS

September 2020

Acknowledgements

This thesis was carried out between the period of February 2020 and August 2020 at the National Hellenic Research Foundation, Institute of Chemical Biology, Medicinal Chemistry & Biotechnology, in Athens.

I would like to express my greatest and sincerest gratitude to Professor Mouzakis, for giving me the opportunity to work in Christos Chochos' group on the very promising field of conjugated polymer nanoparticles. I would also like to thank Dr. Chochos, my research supervisor, for the patience, encouragement and trust that he has placed in me throughout this master thesis. His guidance, educational skills and unlimited motivation were indispensable for the completion of my thesis. I would also like to greatly thank the other two members of my committee, Professor Hermis Iatrou and Associate Researcher Nefeli Lagopati for their very valuable advice, scientific knowledge and time spent on my thesis. Moreover, I was very fortunate to collaborate with the very dedicated partners; Dr. Alkmini Negka and Dr. Panagiota Koralli, from the German Cancer Research Center, Clinical Cooperation Unit Nuclear Medicine, located in Heidelberg, Germany. Their support and valuable advice were very crucial to my successfully completing my thesis.

It would be impossible not to thank Dr. Xenakis and his research group for their excellent technical assistance with the Dynamic Light Scattering (DLS) instrument. I would finally like to express my gratitude towards my family, for their support during this thesis and encouragement in every educational and scientific step that I have made so far.

Abstract

Successful implementation of the encapsulation and nanoprecipitation approaches leads to the formation of water-soluble conjugated polymer nanoparticles (CPNs) which have recently gained considerable attention due to their unique opto-electronic properties. Their application in the biological field is attributed to their simple synthesis and purification procedures as well as their advantageous high brightness, excellent photostability, low cytotoxicity, strong NIR absorbance and versatile functionalization possibilities. By that means, the near-infrared absorbing conjugated polymers, poly [6,7 diphenyl-4-(4,4,9,9-tetrakis(4-hexylphenyl)-4,9-dihydro-s-indacenol[1,2-b:5,6 b′] dithio phen-2-yl)-[1,2,5] thiadiazolo[3,4—g]quinoxaline] (IDTTDQ-Ph) and poly [6,7 diphenyl-4-(4,4,9,9-tetrakis(5-hexylthiophen-2-yl)-4,9-dihydro-s-indacenol[1,2-b:5,6-b′] di-thiophen-2-yl) [1, 2,5]thiadiazolo[3,4—g]quinoxaline] (IDTTDQ-Th), have been investigated as contrast agents for photoacoustic bioimaging, an emerging high resolution and deep penetration depth technique. Lipophilic π-conjugated polymers were efficiently encapsulated within self-assembling diblock copolymer poly(ethylene glycol) methyl ether-*block*-poly(lactide-*co*-glycolide) (PEG–PLGA) nanoparticles and were characterized with UV-Vis spectroscopy, dynamic light scattering and z potential, showing the very promising NIR II absorbance and a biologically acceptable size around 100nm. Lastly, the photoacoustic signal of the encapsulated IDTTDQ-Th and IDTTDQ-Ph conjugated polymer nanoparticles was recorded.

Table of Contents

List of Figures

List of Tables

1. Introduction

1.1 Conventional Clinical Imaging Modalities

Clinical imaging of human patients is routinely carried out in hospitals to diagnose and monitor diseases, guide surgical interventions and evaluate therapy response, planning and recurrence. As far as cancer is concerned, the second leading cause of death globally, the conventional Imaging Modalities for its detection include, computed tomography (CT), magnetic resonance imaging (MRI), positron emission tomography (PET), single-photon emission computed tomography (SPECT), ultrasound scanners and the least predominant optical imaging -and probes (contrast agents)[1-3]. Figure 1, shows the present-day role of imaging in cancer management, that includes screening, diagnosis, treatment and follow up care, while improved awareness and access to care could contribute to early detection of cancer[4] and as a result a significant reduction in mortality for certain cancers can be achieved. Most clinical imaging modalities are based on the interaction of ionizing or non-ionizing electromagnetic radiation with body tissue and fluids. Optical techniques are also emerging with promising outcomes for molecular imaging. Moreover, recent advances in cancer molecular imaging were successfully made through the integration of various imaging modalities, (PET-CT, PET-MRI, MRI-optical, etc.)[5] in order to synergistically enhance, overall sensitivity and specificity as well as clinical decision making. Imaging systems vary in physical properties including sensitivity, temporal and spatial resolution. Figure 2 shows the relative sensitivity of different imaging technologies. As shown in Figure 2, PET and nuclear medicine are the most sensitive clinical imaging techniques with between nanomole/kilogram and picomole/kilogram sensitivity. X-Ray systems including CT have millimole/kilogram sensitivity whereas MRI has about 10 μmol/kg sensitivity. Clinical optical imaging has limited applications for now as well as nanosystems but the figure shows clearly their potential superior sensitivity. In addition, the aforementioned conventional imaging modalities will be shortly discussed.

Figure 1. The present-day role of imaging in cancer management.[1]

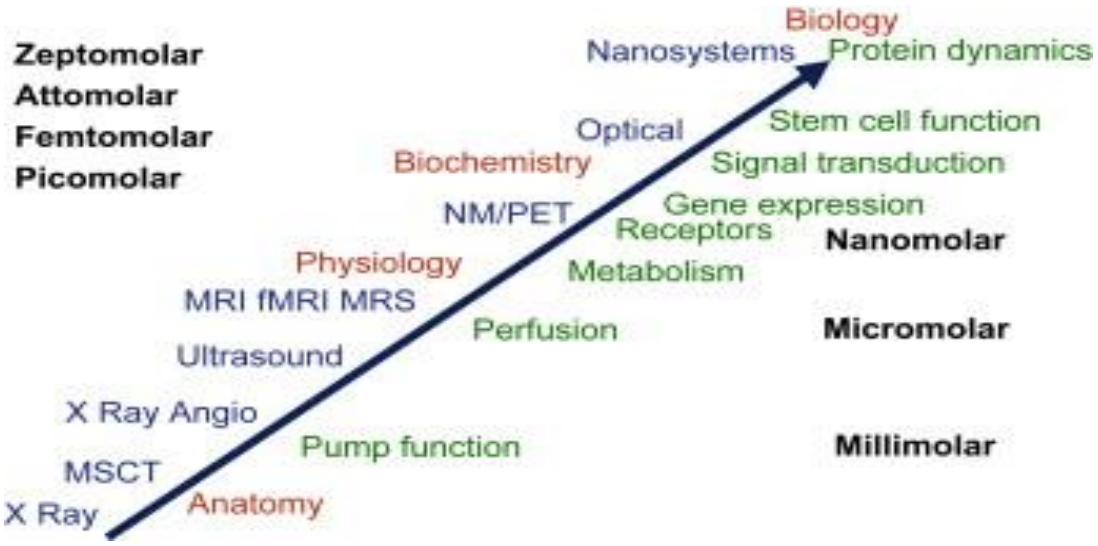

Figure 2. The relative sensitivity of different imaging technologies.[1]

Ultrasound:

Ultrasound (US) imaging is usually applied as an alternative for tumor resection control, on account of its relative small cost, portability, and real-time images. Ultrasounds send out sound waves that bounce against organs and reverberate back to a device called a transducer. The transducer processes the reflected waves and converts them into an image of the targeted organs or tissues, projected onto a computer screen. The sound waves travel at varying speeds, depending on the type of tissue under examination. The sound waves echo off abnormal tissue differently than they do healthy tissue, allowing doctors to distinguish tumors from normal cells. However, due to its low contrast, speckle artifacts, and high operator dependence, the reliability of US imaging is not fully proven. Taking advantage of strong endogenous and exogenous optical contrasts, pure optical imaging has been intra-operatively applied to map tumor margins. However, due to strong light scattering, pure optical imaging suffers from either shallow penetration depth (optical microscopy) or poor spatial resolution (diffuse optical tomography). Along with the application of new imaging techniques, contrast agents have been intensively investigated to improve the degree of resection and preserve normal tissues. Therefore, there is a pressing need to develop a highly sensitive and high resolution imaging tool with proper contrast agents for monitoring surgical resection of intracranial tumors. The application of microbubbles (MBs) in contrast-enhanced ultrasound (CEUS) has become an indispensable part of clinical ultrasonography, and molecular imaging via ultrasound has recently attracted significant attention. MBs help to enhance the specificity and sensitivity of imaging for various types of diseases, especially with tumors. Other advantages of using MBs include a lower cost of contrast agents, an opportunity for real-time observation and the elimination of the exposure to radiation.[6]

X-Ray Imaging- CT scan:

Originally, X-rays were used for imaging bones because they were easily distinguishable from soft tissues on films available at the time. Today, improvements such as better photographic films, more accurate focusing systems and more sensitive detection methods have led to better imaging technology and results. Using lower-exposure levels, fine detail and subtle differences may be distinguished in tissue density. Advances in technology have led to the development of computed tomography (CT) which combines multiple X-ray images into a 3-D model and providing anatomical information of the body with high contrast quality. A valuable medical tool, the X-ray is a non-invasive procedure used for diagnosing disease, monitoring therapy and planning surgical treatment. X-rays may also be used in guiding the placement of medical devices, such as catheters and stents. To help identify a specific area of the body on an image, a contrast medium like barium or iodine may be given to patients undergoing certain types of X-rays. In low doses, X-rays may be used to capture images of structures inside the body to detect and stage a tumor. In addition, the radiation exposure from an X-ray for imaging is low and research suggests the benefits far outweigh the risks. In higher doses, X-rays may be used in radiation therapy to help destroy cancerous cells in the body. X-ray imaging is considered the most commonly used medical imaging modality, since it is more time and cost efficient as compared with MRI and PET.[7]

Magnetic Resonance Imaging (MRI):

MRI is one of the most powerful non-invasive diagnostic techniques applied for whole body imaging. The technology is based on the relaxation of proton spins in a magnetic field. The signal intensity in MRI corresponds to the magnetic relaxation rate of water protons. Under a strong static field B_0 (ranging from 1.5 to 3 Tesla (T) in clinic and 7 T or higher in laboratories), unpaired nuclear spins align themselves with the field in either a parallel or an anti-parallel orientation. An electromagnetic radiofrequency pulse is applied to change the alignment of the spins. The flipped spins tend to return to their original state, which is recorded as either longitudinal (T_1 recovery, spine lattice) or transverse (T_2 decay, spine spin) relaxations. Water protons in different tissues or organs have different relaxation times, resulting in the endogenous MRI contrast. T_1 recovery leads to a brighter image due to the increase in magnetic signal, but T_2 decay reduces the imaging intensity. Introduction of appropriate exogenous contrast agents will help to accelerate the relaxation time of either T_1 or T_2, thereby further enhancing the local contrast. Abnormalities of tissues appear as darker (T_1-weighted) or brighter (T_2-weighted) than healthy tissues, due to differences in relaxation times. The majority of MRI contrast agents are either paramagnetic gadolinium ion complexes or super paramagnetic (iron oxide) magnetite particles-T_2 contrast agents. The paramagnetic contrast agents are usually made from dysprosium (Dy^{3+}), the lanthanide metal gadolinium (Gd^{3+}), or the transition metal manganese (Mn^{2+}) -T_1 contrast agent.[7]

PET Scan:

The positron emission tomography (PET) scan generates computerized pictures of chemical changes occurring in tissue, such as sugar metabolism. Both, nuclear imaging modalities, positron emission tomography (PET) and single-photon emission computed tomography (SPECT) rely on their incorporation of a short-lived radioisotope(emitting positrons for PET and gamma rays for SPECT) into a molecular species (peptide, monoclonal antibody, small organic molecule, nanoparticle) and allow for dynamic quantification of such radiolabeled agents non-invasively due to their high sensitivity (10^{-11}–10^{-12}M). A wide range of isotopes are available, with different decay properties, chemical compatibility and half-life. Commonly used tracers for PET are: ^{18}F, ^{13}N, ^{11}C, ^{15}O, ^{82}Rb, ^{68}Ga, and ^{64}Cu. Dual modality systems like PET-MRI provide a combination of high spatial resolution (MRI) and high sensitivity (PET) system. Moreover, PET scans may be helpful in evaluating and staging recurrent disease and are also commonly used to check if a treatment is effective.[7]

SPECT Scan:

SPECT is another nuclear imaging technique using gamma rays emitted by radionuclides. Similar to conventional nuclear planar imaging, SPECT imaging is performed by using a gamma camera to acquire multiple two-dimensional (2D) projection images from multiple angles. After tomographic reconstruction of multiple 2D views, three-dimensional distribution of the nuclear probes in vivo can be freely reformatted as required. However, the detection efficiency of SPECT imaging is generally much lower than that of PET imaging because of the use of rotating detectors and collimators to reject many gamma photons. The spatial resolution of SPECT is also generally lower. The available gamma emitting radionuclides for SPECT are usually inexpensive, including ^{99m}Tc, ^{111}In, $^{123/125/131}$I.[7]

1.2 Optical (Pre) Clinical Imaging Modalities

Conventional tomographic imaging modalities suffer from considerable limitations that include, adverse effects to hazardous ionizing radiation (CT, PET and SPECT), intrinsically limited spatial resolutions (PET), reconstruction-dependent poor temporal resolution (CT, MRI, PET and SPECT) and lack of both exogenous and endogenous probes for molecular or functional imaging. On the other hand, one of the most inexpensive and rapid methods for imaging at a molecular level is optical imaging which involves; fluorescence and luminescence imaging techniques, in vivo Raman imaging and photoacoustic imaging (PAI).

To begin with, *in vivo* fluorescence-imaging overcomes tomographic imaging modalities' main drawbacks and instead provides the benefits of real-time, wide-field image acquisition and diffraction-limited, spatial resolution, in living organisms through the interaction of non-hazardous optical radiation (usually a monochromatic light source such as a laser or a lamp with a properly installed excitation filter) with a fluorescent agent. An emission light detector and image-forming optics generate a visual representation of the imaged object on the basis of the spatiotemporal distribution of fluorescent labels, which are either exogenously introduced or endogenously expressed to impart contrast to anatomical structures, biological molecules and physiological functions. *In vivo* fluorescence imaging using traditional wavelengths in the visible spectrum, compromises resolution and contrast with increasing tissue depths due to the substantial photon scattering and/or photon absorption by biological tissue, coupled with significant interference from tissue autofluorescence. Subsequently, in comparison with the visible spectrum extensively employed for fluorescence imaging — partly owing to the wide availability of fluorophores in this window — the broadly defined NIR window (700–1,700 nm in wavelength) can afford deeper tissue optical imaging with improved signal-to-background ratio at increased tissue depths.

Fluorophore	Excitation/emission wavelength	Tissue targets	Properties	Applications	Phase
Indocyanine green	807/822 nm	Plasma lipoprotein and atheromas; mostly non-specific	Negatively charged; lipophilic; QY=9.3% (serum)	Cardiovascular and lymphatic angiography; bile duct and GI tract imaging; tumour imaging and IGS	FDA-approved*
MB	665/686 nm	Non-specific	Positively charged; QY=9.6% (serum)	Cardiovascular and lymphatic angiography; bile duct, GI tract and ureter imaging; tumour imaging and IGS	FDA-approved
IRDye800CW	774/789 nm	Non-specific; conjugatable with targeting ligands	Negatively charged; hydrophilic; QY=12% (serum)	Tumour imaging and IGS	Phase I
Non-sulfonated cyanine dyes (CyX Series)	747/774 nm (Cy7) 788/808 nm (Cy7.5)	Non-specific; conjugatable with targeting ligands	Positively charged; QY=28% (Cy7, PBS)	Structural and functional imaging of tumour and other tissues and organs	Mostly preclinical†
Zwitterionic cyanine dyes	772/788 nm (ZW800-1)	$\alpha_v\beta_3$ (with RGD)	Zwitterionic (neutral net charge); hydrophilic; QY=15.1% (serum)	Tumour imaging	Phase I
Phosphonated cyanine dyes	771/796 nm (Pam78) 785/802 nm (P800SO3)	Hydroxyapatite deposits and bone tissues	QY=15.1% (P800SO3)	Bone and microcalcification imaging	Preclinical
Quaternary ammonium cyanine dyes	666/692 nm (C700-OMe) 770/804 nm (C800-OMe)	Cartilage tissues	Hydrophilic; QY=9.7% (C700-OMe), 11.5% (C800-OMe)	Cartilage imaging	Preclinical
BODIPY	643/673 nm (mPB) 649/723 nm (BAP-5)	Non-specific (mPB) Amyloid beta plaque (BAP series)	Charge-neutral; hydrophobic BODIPY core; QY~100% (water)	Tumour and Alzheimer's disease imaging	Preclinical
Conjugated copolymers	500–1,100/ 700–1,400 nm	Non-specific; conjugatable with targeting ligands	Hydrophobic; QY=0.5–50%	Structural and haemodynamic imaging of blood vasculature, lymph nodes and tumour	Preclinical
Aggregation-induced emission dots	511/671 nm (TPE-TPA-FN AIE dot)‡	Non-specific; conjugatable with targeting ligands	Hydrophobic; QY=12.5% (TPE-TPA-DCM at 3 wt% loading in BSA)	*Invivo* cell tracking and tumour imaging	Preclinical
Quantum dots	Declining broadband absorption/ 700–1,500 nm emission	Non-specific; conjugatable with targeting ligands	QY=8–17%	Cardiovascular and lymphatic angiography; tumour and skeletal imaging; lymph-node mapping; visualization of cell migration; *invivo* thermometry	Preclinical
Metal nanoclusters	360/810 nm (Au)	Non-specific; conjugatable with targeting ligands	Highly water-soluble; QY=0.7% (Au)	Imaging of tumour, kidney clearance kinetics and kidney dysfunction	Preclinical
Infrared fluorescent proteins	690/711 nm (IFP2.0) 674/703 nm (miRFP703)	Liver (with adenovirus vector) or specific molecular targets	Expressed endogenously; QY=8.0% (IFP2.0) and 8.6% (miRFP703)	Imaging of liver, brain tumour, myoblast differentiation, muscle regeneration, cancer metastasis, signalling cascade, cell cycle and specific protein labelling	Preclinical
Single-walled carbon nanotubes	550–1,050 nm multiband/ 1,000–1,800 nm multiband	Non-specific; conjugatable with targeting ligands	Inherently hydrophobic; QY=0.4%	Imaging of internal organs, tumour, limb and brain vasculatures, lymphatic vessels and lymph nodes, bacterial infection and nitric oxide	Preclinical
Rare-earth nanoparticles	808 or 980/ 1,000–1,600 nm	Non-specific; conjugatable with targeting ligands	QY=90% (SrF2:Nd), 50% (LaF3:Nd)	Imaging of blood vasculature, internal organs and tumour	Preclinical

Figure 3. Common NIR-I and NIR-II fluorophores.[2]

Therefore, the need for deep-tissue and real-time fluorescence imaging calls for advances in basic science through the development of both imaging instrumentation and new fluorescent probes.

Up to now, the most widely developed Fluorescence/PA agents are inorganic nanomaterials such as noble metal nanomaterials (e.g., Au and Pd), transition metal dichalcogenides (e.g. MoS_2, WS_2 nanosheets, and CuS_2 nanoparticles), and carbon nanomaterials (e.g. graphene and carbon nanotubes). However, a potential concern is that these typical non-biodegradable inorganic nanomaterials could remain in the body for a long period of time, which could lead to potential long-term biotoxicity and significantly hindering potential *in vivo* applications. As a result, the development of organic nanomaterials for clinical imaging is of great demand. This kind of materials will be discussed later.[2,7]

Photoacoustic imaging:

Photoacoustic imaging, also known as optoacoustic imaging, is a truly fused multi-imaging modality. It has emerged over the last decade, and is based on the use of laser-generated ultrasound. It holds great promise for clinical translation and possesses several unique advantages over many other imaging modalities. As a promising non-ionizing, non-invasive and highly sensitive molecular imaging technique, PAI takes advantage of both optical and acoustic imaging, and thus overcomes the depth limitation of most traditional optical imaging techniques. The photoacoustic effect was first observed in 1880 by Alexander Graham Bell. It is based on the generation of ultrasound waves by a light-absorbing material following the absorption of modulated light, usually pulsed laser light on a nanosecond timescale. Basically, the optical energy is absorbed and partially converted into heat, resulting in transient thermo elastic expansion and thus ultrasonic emission, which is then detected by ultrasonic transducers to form images. Moreover, PAI provides functional and molecular information of tumors in real time with high imaging contrasts and ultrasonic spatial resolution through either endogenous or exogenous PAI contrasts. Due to available intrinsic contrast molecules, such as hemoglobin or melanin, PAI has been used to visualize blood vessel structure, thermal burns, and melanoma for tumor angiogenesis monitoring, blood oxygenation mapping, functional brain imaging, and skin melanoma detection. However, most diseases such as cancers do not show good PA contrast using endogenous PAI molecules,

thereby it is necessary to develop new exogenous contrast agents which could provide sufficient PA signal even in low concentrations.[7,8]

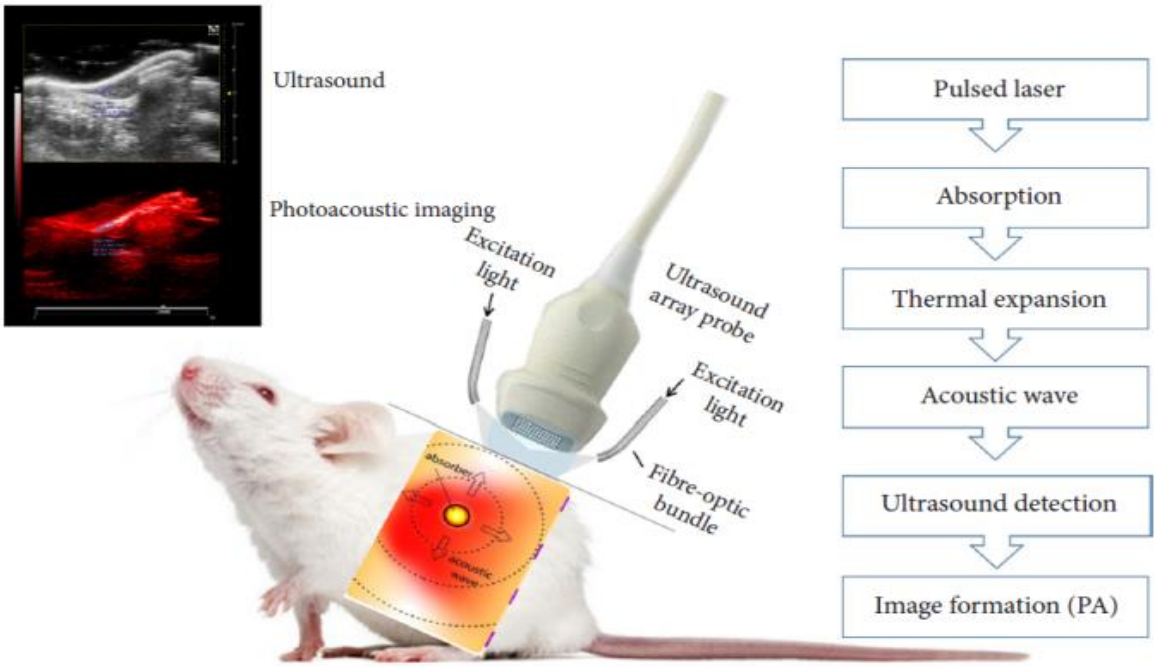

Figure 4. The basic principle of photoacoustic imaging.[8]

As shown in Figure 4 above, when a tissue is exposed to pulsed near-infrared laser light, the constituents of the tissue (e.g., water, lipids, collagen, hemoglobin, etc.) absorb light and undergo thermoelastic expansion, thereby causing ultrasound signals to emanate (the photoacoustic effect). Therefore, these laser-induced ultrasound signals (photoacoustic signals) can be detected using an ultrasound transducer, making photoacoustic imaging possible. Each of these biological absorbers can be targeted by irradiating tissue at the corresponding dominant absorption wavelength. As such, using a tunable laser at the relevant wavelengths of interest enables the acquisition of multiple photoacoustic images that can be spectrally resolved for tissue composition to be assessed based on endogenous contrast. PA, photoacoustic.

1.3 Nanoparticles for imaging applications

Nanomaterials have attracted more and more attention over the last few decades due to their distinct and superior chemical and physical properties from their bulk materials. A nanomaterial is referred to as “a natural, incidental or manufactured material containing particles in an unbound state or as an aggregate or as an agglomerate and where for 50 % or more of the particles in the number size distribution, one or more external dimensions is in the size range 1-100 nm”. Nanoparticles designed for biomedical applications can be found in the full nanoscale size range; however, in practice, nanoparticles with diameters of 5-250 nm typically present beneficial properties. In particular, the high surface to volume ratio of nanoparticles enables the versatility of surface functionalization and enhanced reactivity. Besides, particles in nanoscale resemble the size of biological molecules or structures. The nanoparticle shape, size, chemical composition and surface properties play an important role in its cellular uptake, clearance and biodistribution. All of these merits contribute to the widespread studies and applications of nanoparticles in biomedical research including sensors, nanomedicines and molecular imaging agents. As far as the molecular imaging is concerned, in an attempt to improve the performance of imaging procedures, the most commonly used nanoparticles are inorganic nanoparticles (such as metal NPs, carbon nanotubes, metal oxide NPs, quantum dots) and organic nanoparticles (liposomes, polymeric vesicles, π-conjugated polymers). Inorganic nanoparticles’ wide-ranged use can be attributed to their superior optical, electrical and magnetic properties, leading to significant enhancement in imaging contrast. Among various nanoparticles, super paramagnetic iron oxide nanoparticles have been used as contras agents for MRI. Gold-based nanoparticles, such as gold rods, gold nanoshells and gold nanocages, have been extensively investigated due to their unique surface Plasmon resonance (SPR) in optical imaging, Raman spectroscopy and photoacoustic imaging. Quantum dots have recently received immense attention in cancer imaging because of their very promising fluorescent properties. Compared to conventional molecular platforms used for imaging, the use of nanoparticle-based molecular probes shows several distinctive advantages and has great potential in both non-invasive detection as

well as the treatment monitoring of human cancers. Firstly, multifunctionality is a key advantage of nanomaterial-based imaging probes for cancer diagnosis. Through systematic conjugation with different targeting moieties, contrast enhancers, permeation enhancers, or even therapeutic agents, various molecular imaging nanoprobes can bypass biological barriers, achieve the capability to recognize tumor specific biomarkers, and visualize and quantify tumor growth or regression during therapy with improved imaging sensitivity and specificity can potentially alter and improve the pharmacokinetics of molecular probes in vivo. Moreover, by coating nanomaterials with biocompatible polymers, the circulation half-life of molecular probes can be extended to have more opportunities to penetrate though vascular endothelium and reach the desired sites while minimizing uptake by the reticuloendothelial system (RES).[7,9,14]

1.4 Conjugated Polymers

The Nobel Prize in Chemistry in 2000 was awarded jointly to Alan J. Heeger, Alan G. MacDiarmid and Hideki Shirakawa "for the discovery and development of conductive polymers". Since then, the versatile class of polymeric materials has gained tremendous interest from academia and industry. These materials, have been extensively explored for a wide range of applications, spanning from electronics (LEDs) and energy harvesting (solar cells) to nanomedicine (Imaging, theranostics). In fact, with their unique biophysicochemical properties, they are considered to be superior to other classes of nanomaterials, such as small organic dyes, semiconducting quantum dots, and inorganic nanoparticles, in many biomedical applications.[11-15] Small organic molecules generally exhibit low (photo)stability and photobleaching while inorganic nanoparticles are usually challenged with non-negligible toxicity concerns.[16,17] On the other hand, Conjugated polymers, due to their chemical nature are generally stable, non-cytotoxic and their optical properties can be readily tuned.[18-20] By the term conjugated polymer, we describe a polymer with alternating double and single-bonds in the polymer chain. Due to the successive distribution of carbons with π-bonding, conjugated polymers have the ability of electron delocalization and subsequent charge- movement around the whole system. This specific property makes them conductive. Specifically, when electrons are removed from the backbone they act as anions.[21] In order to understand the properties of an organic semiconductor we will use as an example the C-C bond. The electron configuration of carbon is $1s^2 2s^2 2p^2$. Carbon has four electrons in its valence shell (outer shell) and two core electrons ($1s^2$). Atomic orbitals with s-character have spherical symmetry and a representation of the surface of the carbon 1s orbital is shown in Figure 5a.

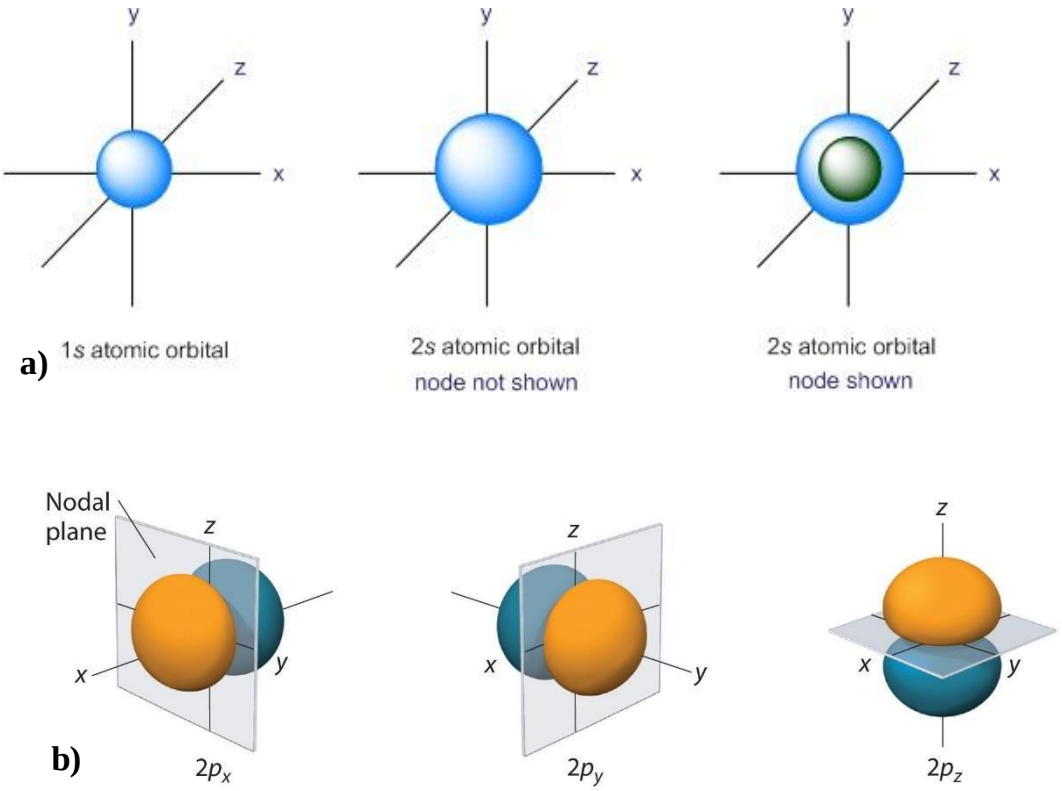

Figure 5 (a,b). A representation of the surface of the carbon 1s and 2s orbitals.[22]

The wave properties of electrons make the description of the 2s orbital slightly more complex than the corresponding 1s orbital, in that, within the 2s sphere there is a region in which the amplitude of the electron standing wave falls to zero, that is, there is zero probability of finding the electron in this node region. Nodes are most easily seen in the description of the 2p atomic orbitals, which are shown in Fig. 5b. The electron densities along the x, y and z axes of the 2p orbitals are clearly shown in the figure; the nodes are the points at the origin and at these points, there is zero probability of finding the electron. The sharing of electrons in a covalent bond occurs by overlap of the individual atomic orbitals. Head-on overlap between energetically compatible orbitals generates sigma (s) bonds, while sideways overlap (typically from adjacent *p* orbitals) generates pi (p) bonds. Examples of sigma and p-bond bond formation between atoms "A" and "B" are shown below (Figure 6).

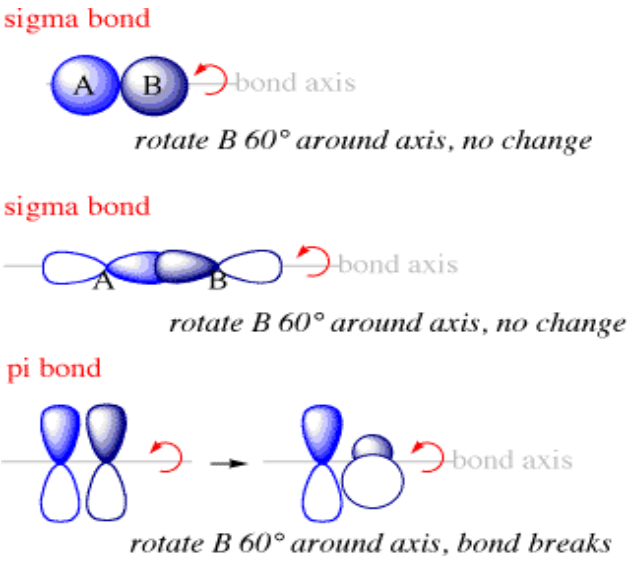

Figure 6. Examples of sigma and p-bond bond formation between atoms "A" and "B".[22]

The nature of the bonding in carbon (C_2) can be described using the Molecular Orbital Theory. As the two atomic orbitals approach each other and begin to overlap, there is a decrease in the net energy of the system because the electrons in each atom tend to become attracted to the positive nucleus of the other atom, as well as their own nucleus. The more the orbitals overlap, the more the energy decreases, until the nuclei approach so closely that they begin to repel each other. The point at which the repulsive and attractive forces balance defines the bond distance for a given covalent bond. In molecular orbital theory, the number of atomic orbitals used to make the covalent bond must equal the total number of molecular orbitals in the molecule. The molecular orbital description of this simple covalent bonding is shown below (Figure 7). As described above, the bonding orbital is referred to as a σ/π-orbital, while the corresponding antibonding orbital is referred to as a σ*/π*-orbital. Overlapping, according to quantum mechanics can be either "efficient", if the fluctuations are in phase, or "destructive" if the fluctuations are out of phase. Thus, respectively, the bonding molecular orbitals and the antibonding molecular orbitals (AMD) arise.

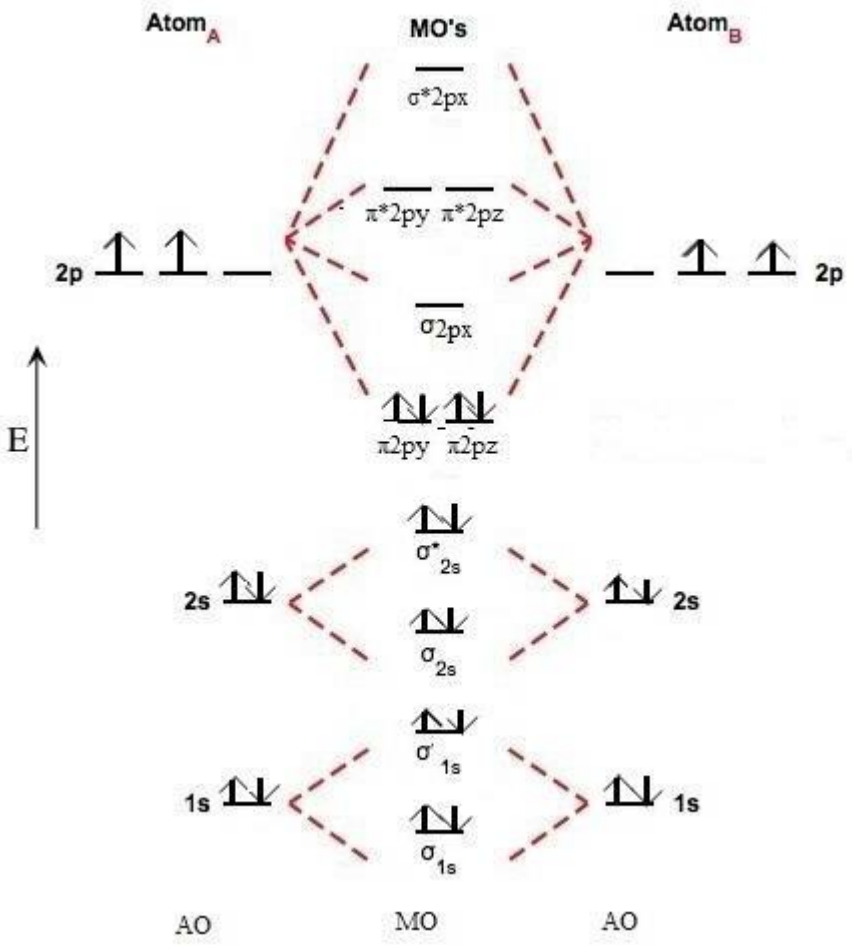

Figure 7. The molecular orbital description of C_2.[22]

Sigma (σ) bonding molecular orbital: Shared electron density is directly between the bonding atoms along the bonding axis. A sigma bond is always the first bond formed between two atoms.

Pi bond (π): bonding molecular orbital :The bonding electron density lies above and below, or in front and in back of the bonding axis, with no electron directly on the bonding axis, since 2p orbitals do not have any electron density at the nucleus.

Sigma star (σ*) and Pi star (π*) antibonding molecular orbital: Normally this orbital is empty, but if it should be occupied, the wave nature of electron density (when present) is out of phase (destructive interference) and canceling in nature. There is a node between the bonding atoms (zero electron density). This produces repulsion between the two interacting atoms, when electrons are present. It is important to mention, that the antibonding molecular orbital is also known as the LUMO (lowest unoccupied molecular orbital) energy level. Only the HOMO (highest occupied molecular orbital) molecular orbital bond is occupied by electrons. The highest energy antibonding molecular orbital (LUMO) is empty.[22]

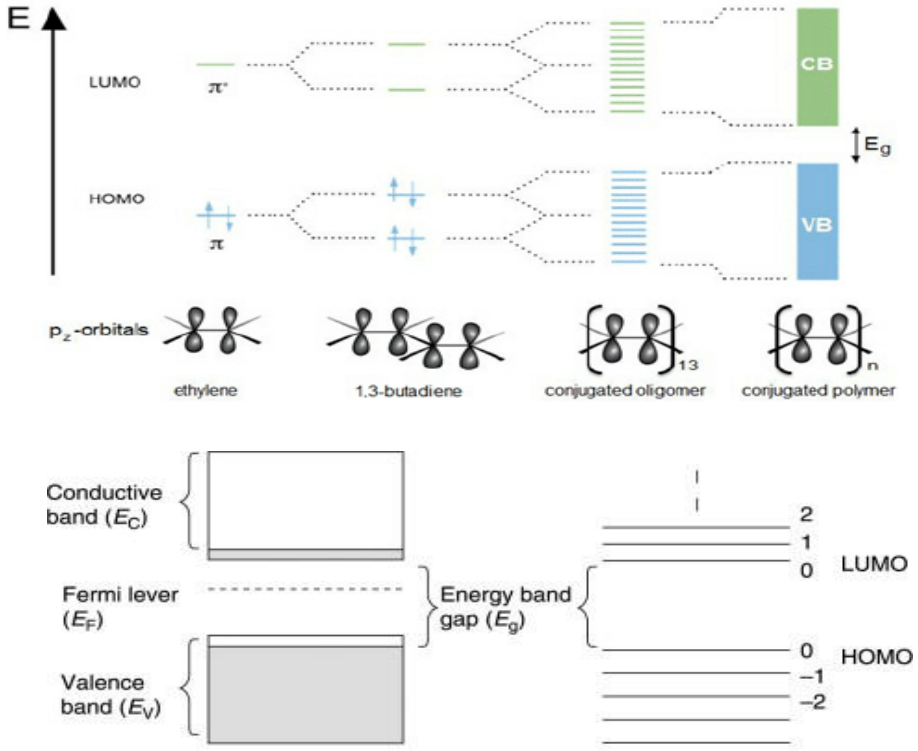

Figure 8. Different HOMO-LUMO band gaps determine the electric conductivity of the polymers.[23]

Conjugated polymers is a category of polymers that consists of alternating repeated subunits that form sigma and pi-bonds.[23] The electric effect that these polymers exhibit is a result of the overlapping of the p_z molecular orbitals (pi conjugation). The extent of overlapping (conjugation length) determines the HOMO-LUMO band gap of these semiconductors (Figure 8). Conjugated polymers also exhibit a wide range of optical properties which are induced by the addition of impurities that act as electropositive or electronegative components. Alterations in the HOMO-LUMO band gap affect the chemical, physical and mechanical characteristics of the conjugated polymers. Generally, the alterations of the HOMO-LUMO bandgap are dependent on six factors; i) the molecular weight of the conjugated polymer (CP), ii) the alternation of the bond length, iii) the rotation angle, iv) the aromatic character of the polymer, v) the size of the substituent groups and vi) the intermolecular interactions. A lot of on-going research focuses on the founding of organic imaging probes that combine high fluorescence, excellent photostability, high brightness, resistance to photo-bleaching, high signal-to-noise ratio, high emission rates, and low cytotoxicity. All these characteristics are ideal for bio-imaging. However, the energy gaps of most polymeric materials are normally greater than 2 eV, covering only the visible range of the electromagnetic spectrum (300-650 nm). Organic materials that possess energy gaps below 1.5 eV are of great demand to extend absorption to the near infrared region of the solar spectrum. Therefore, it has been a major effort to design and synthesize novel conjugated polymers with narrow energy gaps in recent years.[24] For the modification of the Eg and the HOMO and LUMO energy levels of the conjugated polymers, two chemical approaches are applied. The first involves the conversion of a conjugated polymer chain from the aromatic form to the quinoid form (Figure 9) and the second is based on the synthesis of the so-called "donor-acceptor" alternating copolymers containing alternating electropositive and electronegative monomers in the same polymeric chain. Considering the great effects that CPs possess, many scientific groups attempted to modify their hydrophobic properties recently, in order to use them in the field of bioimaging, signaling and theranostics.[23]

Thus, CPNs are capable of a wide range of light absorption spectra characteristics in the red, far-red and near-infrared regions with higher absorption coefficients and photostability as compared to small molecule dyes and their assembled nanoparticle forms. The near infrared spectroscopy-NIRS[25] is a spectroscopic method that uses the near- infrared region of the electromagnetic spectrum (from 780nm to 2500nm). The father of NIRS, William Herschel, discovered it in the 19th century but the first industrial application began in the 1950s. One of the main advantages of the NIR is that it can penetrate much further into the sample than the mid infrared radiation. According to recent publications [24-26], CPNs absorb and emit light energy in the UV- Vis and the NIR region, which can be effectively converted to photoacoustic and fluorescence effects. Such novel imaging probes provide an emission spectral window, also known as therapeutic window. The term therapeutic window was introduced, due to the fact that for wavelengths ranging from 650 to 1350 nm, light has its maximum depth of penetration in tissue. Subsequently, we can assume that with the NIR spectrum scientists could probably interfere to the metabolic profile of the cells. The emission spectral window offers i) high tissue penetration, ii) low autofluorescence and also iii) minimization of various limiting factors including self-absorption and scattering. Absorptions in the NIR region (780-2500 nm) are generated from fundamental vibrations by two processes; i) overtones, which are harmonics and ii) combinations, which are more complex and the NIR absorptions require more energy than a fundamental absorption. More specifically, combinations arise from the sharing of NIR energy between two or more fundamental absorptions. To sum up, conjugated polymer nanoparticles (low-band gap) are considered not only as a-new-generation agent for bio-imaging applications with unique optical properties but also a very promising candidate for sensing of pH, ions and temperature, photothermal ablation of tumors, photodynamic therapy and real-time activation of neurons and more (Figure 10).

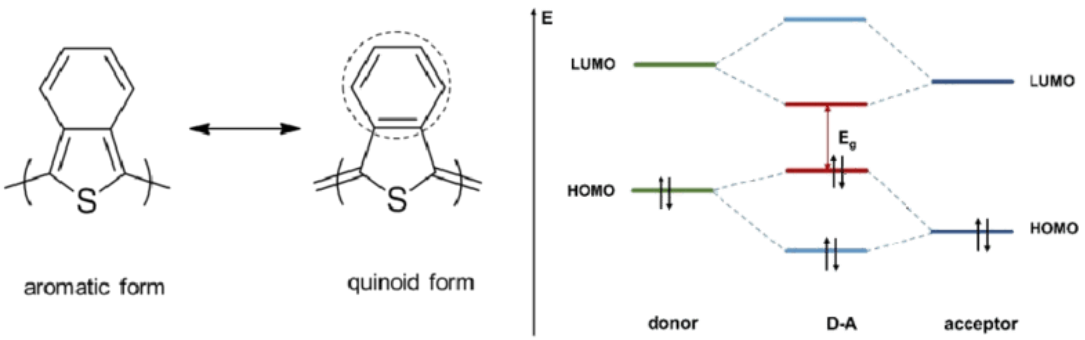

Figure 9. (a) The aromatic and quinoidal forms of poly (isothianaphthene) (b) Simplified molecular orbital hybridization and resulting band gap reduction in D–A conjugate systems.

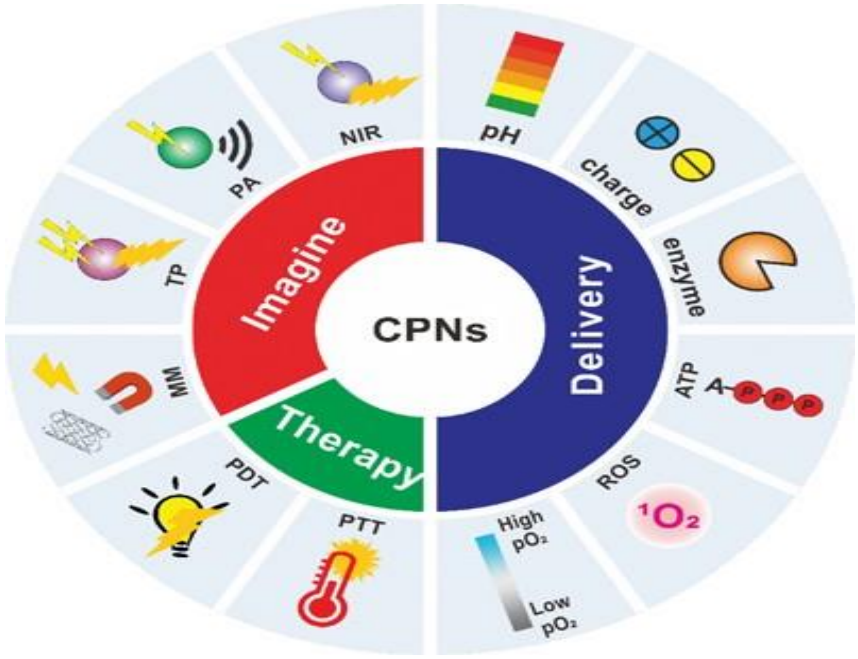

Figure 10. Schematic representation of utilizing conjugated polymer nanomaterials (CPNs) for theranostics.[23]

2. Materials and Methods

2.1 Materials

The reactions carried out are air sensitive and therefore, they were performed under argon. All glassware was washed using detergent (Teepol), rinsed with excess water, acetone and methylene dichloride and dried in an oven at 120^{o}C. All solvents and reagents were purchased from Aldrich. Toluene was distilled using calcium hydride (CaH_2) prior to polymerization. The synthesis of poly [6,7 diphenyl-4-(4,4,9,9-tetrakis(4-hexylphenyl)-4,9-dihydro-s-indacenol[1,2-b:5,6b′]dithiophen-2-yl) [1,2,5]thiadiazolo[3,4—g]quinoxaline and poly [6,7 diphenyl-4-(4,4,9,9-tetrakis(5-hexylthiophen-2-yl)-4,9-dihydro-s-indacenol[1,2-b:5,6-b′]dithiophen-2-yl) [1, 2,5]thiadiazolo[3,4—g]quinoxaline were performed and poly(ethylene glycol)methyl ether-poly(lactide-co-glycolide)(mPLGA-b-PEG) [average molecular weight per number ($\overline{M_n}$) of PLGA is 7000 g mol^{-1}, and that of PEG is 5000 g mol^{-1}] , was purchased from Sigma Aldrich.

2.2. Methods

2.2.1 Synthesis of Conjugated Polymers

Catalytic reactions of aromatic carbon-carbon (C-C) bond coupling are one of the most commonly used organic reactions for the synthesis of several chemical compounds in different scientific fields. New synthetic methodologies are always a critical research topic that is actively pursued. Most recently, polycondensations based on transition metal-catalyzed C-C bond formation reactions have emerged as important methodologies for synthesis of electro -optic materials. These reactions include Stille, Suzuki, Negishi, Heck, and so on.[27-30] The synthetic applications of Stille coupling are immense. Stille coupling has been of great use towards the synthesis of many such products, many of these being antibiotics or anticancer drugs (manzamine A, ircinal A, oxazolomycin etc.). Moreover it is one of the versatile methods for the synthesis of organic functional materials due to its stability, excellent compatibility with various functional groups and high reaction yield. The reaction involves the coupling of two organic groups, one of which is carried as an organotin compound (also known as organostannanes). A variety of organic electrophiles provide the other coupling partner. The Stille reaction is one of many palladium-catalyzed coupling reactions. Some of the advantages of the Stille reaction is i) that the alkyl groups of Sn are easy to synthesize and to store and ii) that it can be combined with a wide range of functional groups iii) very mild reaction conditions. The following scheme shows the reaction's mechanism.

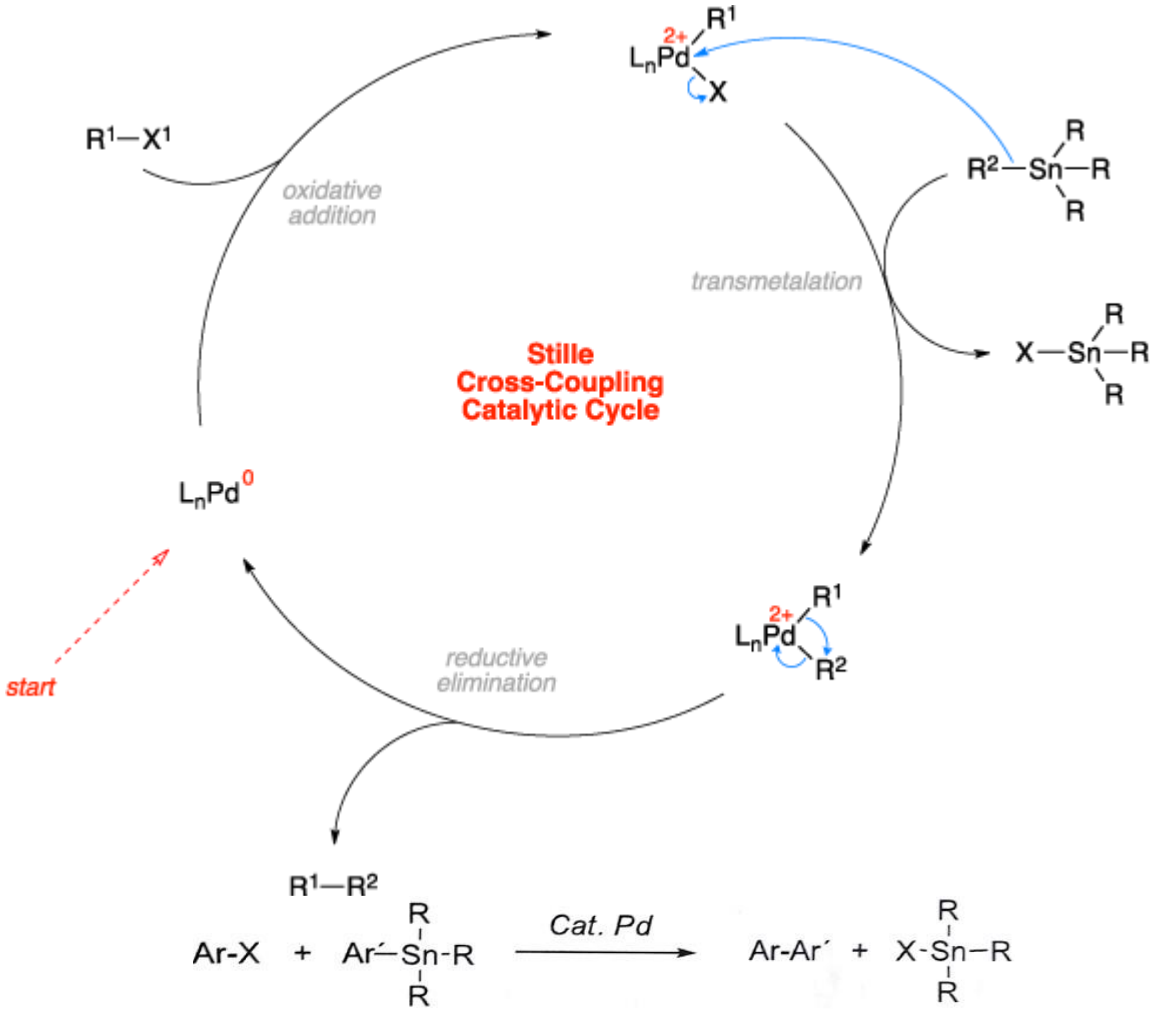

Figure 11. The Stille coupling aromatic reaction.[27-30]

The mechanism of the Stille reaction has been extensively studied. The catalytic cycle involves an oxidative addition of a halide or pseudohalide to a palladium catalyst, transmetalation, with an organotin reagent, and reductive elimination to yield the coupled product and the regenerated palladium catalyst

More specifically, the low-bandgap conjugated polymers were synthesized *via* palladium catalyzed aromatic cross coupling Stille polymerization reaction. For the synthesis, the (4,9-dibromo-6,7diphenyl-[1,2,5]thiadiazolo[3,4—*g*]quinoxaline) (1 equiv.) was combined with either, the monomer (4,4,9,9-tetrakis(4-hexylphenyl)-4,9-dihydro-s-indacenol[1,2-*b*:5,6-*b*′]dithiophene-2,7-diyl)bis(tri –methylstannane)) (1 equiv.) for the IDTTDQ-Ph or

the monomer (4,4,9,9-tetrakis (5-hexylthiophen-2yl)- 4,9-dihydro-s-indacenol [1,2- *b*:5,6-*b*'] dithiophene-2,7-diyl) bis (trimethylstannane)) (1 equiv.) for the IDTTDQ-Th polymer. Then, dry toluene (0.025M) was added to the reaction mixtures. Finally, tris (dibenzylideneacetone) dipalladium(0) [$Pd_2(dba_3)$] (0.029 equiv.) and tri(o-tolyl)-phosphine [$P(o\text{-}tol)_3$] (0.116 equiv.) were added and the reaction mixture was stirred at 120 ^{o}C under an argon atmosphere for 48 h in the case of IDTTDQ-Th and both 1h and 24h reaction time, in the case of IDTTDQ-Ph. As a result a lower ($\overline{M_n}$) (IDTTDQ-Ph-LMW) and a higher ($\overline{M_n}$) would occur (IDTTDQ-Ph-HMW). The polymers were purified by precipitation in methanol, filtered and washed using a Soxhlet apparatus with methanol, acetone, hexane and chloroform. The chloroform fractions were evaporated under reduced pressure and the polymers were precipitated in methanol, filtered through a 0.45 mm PTFE filter and finally dried under high vacuum, rendering a black solid for the IDTTDQ-Th, IDTTDQ-Ph-HMW. The reaction yields of the resulting polymers are 68% (IDTTDQ-Th), 76% (IDTTDQ-Ph-LMW) and 17% (IDTTDQ-Ph-HMW) respectively.

2.2.2 Preparation of Nanoparticles

Generally, CPs are hydrophobic, and thus significant improvement of their water solubility is required in order for them to be applied for *in vitro* and *in vivo* applications. The two major approaches followed for the preparation of aqueous CPNs are the nanoprecipitation and the encapsulation method.[31] In the first approach, often termed as the reprecipitation or injection method, the conjugated polymer is dissolved in a good (non-polar) solvent. The solution is then dispersed in a (polar) solvent, which is a poor solvent for the conjugated polymer, where either droplets of the polymer solution are formed or the polymer precipitates. In the second approach, amphiphilic PEGylated block copolymers are popularly utilized to encapsulate conjugated polymers in order to enhance the biocompatibility of nanomaterials, so that their wider application in imaging and therapy will be achieved.[31,32,33]

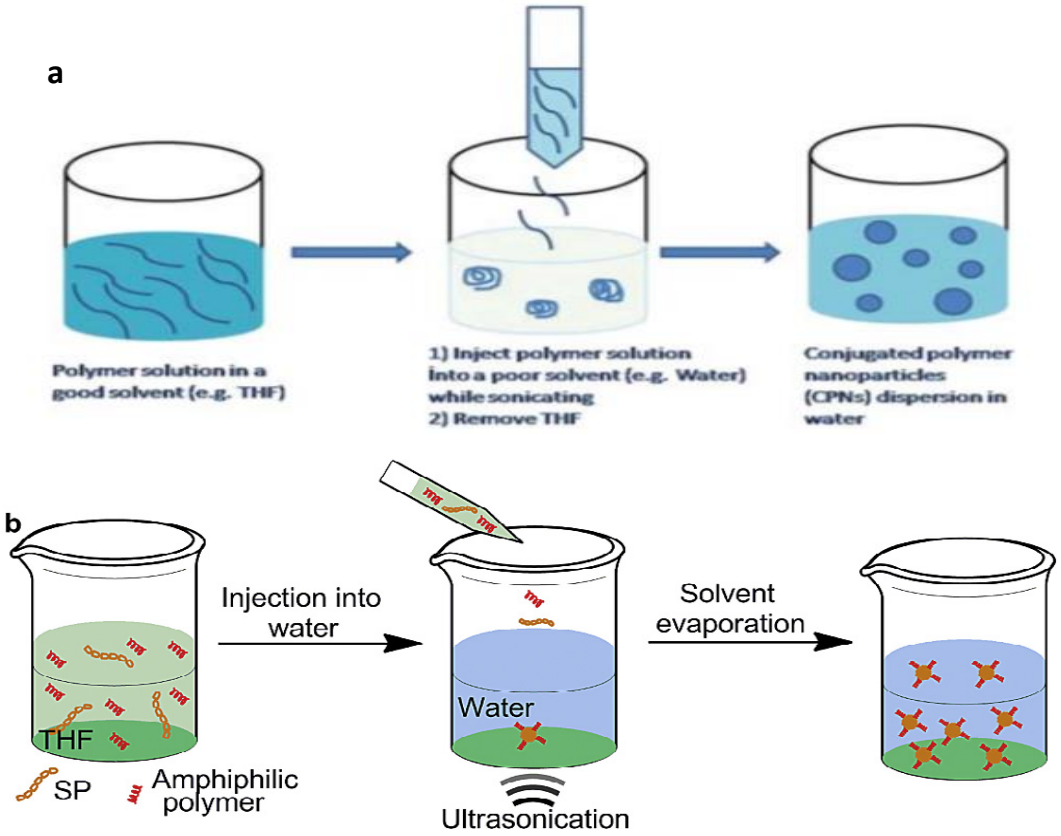

Figure 12. The nanoprecipitation [32](a) and the encapsulation[33] (b) process.

(a) Nanoprecipitation protocol:

1. Each CP was dissolved in tetrahydrofuran (THF) at a concentration of 0.02 mg mL^{-1}.
2. A different portion (from 0.5 mL to 1.0 mL on a case-by-case basis) of each polymer solution (stock solution) was added dropwise to 7 mL of deionized water, under sonication at room temperature, until aggregates are formed.
3. The solutions were then left overnight to allow complete evaporation of the THF and the volume of water lost was replaced.
4. The obtained CPNs were then filtered through a 0.2 μm cellulose acetate filter.

The resulting concentrations (before filtration) of the CPNs were 1.7 ppm for the IDTTDQ-Th polymer and 5.7 ppm for the IDTTDQ-Ph-LMW polymer.

(b) Encapsulation protocol:

1. 1 mg of each CP and a varied amount of 1-10 mg of poly(ethylene glycol)methyl ether-block-poly(lactide-co-glycolide) (mPEG-b-PLGA) were dissolved in 1 mL of THF.
2. The resulting solutions were added dropwise to 7 mL of deionized water, under sonication, at room temperature.
3. The solutions were then left overnight to allow complete evaporation of the THF and the volume of water lost was replaced.
4. The obtained CPNs were centrifuged for 5 minutes (1000rpm) and then filtered through a 0.2 μm cellulose acetate filter.

The resulting concentration (before filtration) was 143 ppm for the IDTTDQ-Th NPs.

For the encapsulated IDTTDQ-Ph NPs, various quantities were examined but the 700μl seems to be the most promising one leading to a final concentration of 100ppm in water.

2.3 Instrumentation

2.3.1 Nuclear magnetic resonance (^{1}H- NMR). ^{1}H-NMR measurements were carried out in solutions (1% w/v) of the copolymers using $CDCl_3$ (Acros 99.6%) as the solvent and tetramethylsilane (TMS) as the integral standard on a Varian 600 MHz NMR spectrometer at ambient temperature.

Figure 13. Varian 600 MHz NMR spectrometer.

The ^{1}H NMR proton spectrum, which is extensively used to study the stereochemical representation of polymers, consists of a group of spectral lines due to the different proton types of the sample. From one spectrum three basic information is obtained; i) the position of the spectral line or chemical shift, which is characteristic of the type of particles, ii) the area of the area under each spectral line, which is proportional to the number of particles present in the sample and, finally, iii) the range of the spectral line associated with the molecular proton of the particular proton[35,36].

The coordination of each nucleus at a different frequency is due to the existence of electrons surrounding it. These electrons create local magnetic fields that protect it, causing the core to feel a Bloc field other than the applied B.

$B_{loc} = B (1 – \sigma)$ (2.3.1)

where σ, (the shielding or screening constant), a dimensionless quantity that determines the electronic density around the core and hence its degree of protection.

The chemical shift of a core is the difference between the core resonance frequency and a standard reference substance. The reference substance for the proton spectrum is tetramethylsilane ($Si(CH_3)_4$), TMS, which has twelve equivalents and highly protected protons. The chemical shift δ is defined by the following equations:

$$\delta = \frac{B_\alpha - B_\delta}{B_\alpha} \times 10^6 ppm \qquad (2.3.2)$$

$$\delta = \frac{\nu_\alpha - \nu_\delta}{\nu_\alpha} \times 10^6 ppm \qquad (2.3.3)$$

where B_α and B_δ are the co-ordinating regions of the reference and sample cores, respectively. V_α and V_δ are the frequencies of the reference substance and the sample, respectively. The more defended a core is (a high value of σ), the resonance will be achieved in highly applied magnetic fields and at a lower frequency. The fact that the area under the spectral line is proportional to the number of particles in the sample is the basis of the quantitative analysis. From the ratio of different spectral lines, which are due to different kinds of particles, the composition of the copolymers can be determined. Finally, the degree of peak breaking allows for its identification. The number of spectral lines obtained is 2nxIx + 1, where nx is the number of equivalent neighboring cores and Ix the spin of the kernel. In the case of 1H and 13C, where spin is I = 1/2, the above relation is nx + 1. The relative peak intensities are the coefficients of the terms of the distribution (1 + x) n. A nucleus separated by two other adjacent nuclei, for example, will give a triple peak with 1: 2: 1 peak intensities.

2.3.2 Gel permeation chromatography (GPC). Average molecular weights per number ($(\overline{M_n})$) and polydispersity indices (*D*) were determined with GPC, on a Shimadzu liquid chromatography (LC-20AD) system consisting of a DGU-20A5R degassing unit, a SIL-20AC HT auto sampler, a CTO-20AC column oven, aSPD-20AV UV-Vis detector and a RID-20A refractive index detector connected in series. The system contains a PL-GEL 10 µm guard column, two PL-GEL 10 µm Mixed-B columns.

The instrument was calibrated with narrow polystyrene standards with M_p ranging from 580 g mol^{-1} to 1.074 kg mol^{-1}. Chloroform was used as the solvent for the GPC measurements.

Figure 14. Shimadzu liquid chromatography (LC-20AD).

2.3.3 Dynamic light scattering (DLS). Structural study was performed using dynamic light scattering (DLS) in order to determine the mean diameter (d, nm) of the nanodroplets and the polydispersity index (PdI) of the system. DLS measurements were performed using a Zetasizer NanoZS device (ZEN3600) from Malvern Instruments (UK) equipped with a He–Ne (632.8 nm) laser and detection was performed at a scattering angle of 1731.

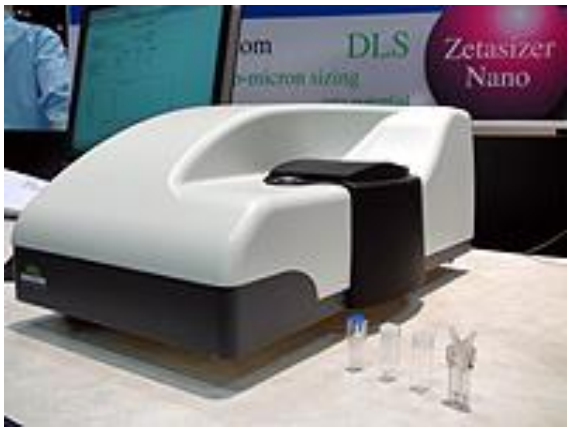

Figure 15. Zetasizer NanoZS device (ZEN3600).

The mean diameter of the dispersed nanodroplets was calculated using the Stokes–Einstein law:

$$R_{\mathrm{H}} = \frac{k_{\mathrm{B}}T}{6\pi\eta D} \qquad (2.3.1)$$

where R_H is the hydrodynamic radii of nanodroplets, k_B is the Boltzmann constant, T is the absolute temperature, η is the viscosity of the microemulsion (in specific temperature) and *D* is the diffusion constant.[37]

After their preparation the microemulsions were placed in a suitable glass cell under dust-free conditions. The experimental data were processed using version 6.32 of the Malvern Zetasizer Nano software (Malvern Panalytical Ltd, Enigma Business Park, UK). The temperature during the measurements was constant at 25°C. Experiments were performed in triplicate for each sample, and the results were presented as average ± S.D. The Dynamic Light Scattering (DLS) method is the most common measuring technique in the nanometer range for particle size analysis. Dynamic light scattering (DLS) is based on the Brownian motion of dispersed particles. When particles are dispersed in a liquid they move randomly in all directions. The principle of Brownian motion is that particles are constantly colliding with solvent molecules. These collisions cause a certain amount of energy to be transferred, which induces particle movement. The energy transfer is more or less constant and therefore has a greater effect on smaller particles. As a result, smaller particles are moving at higher speeds than larger particles. If you know all other

parameters which have an influence on particle movement, you can determine the hydrodynamic diameter by measuring the speed of the particles. The relation between the speed of the particles and the particle size is given by the Stokes Einstein equation The speed of the particles is given by the translational diffusion coefficient D. Further, the equation includes the viscosity of the dispersant and the temperature because both parameters directly influence particle movement. A basic requirement for the Stokes-Einstein equation is that the movement of the particles needs to be solely based on Brownian motion. If there is sedimentation, there is no random movement, which would lead to inaccurate results. Therefore, the onset of sedimentation indicates the upper size limit for DLS measurements. In contrast, the lower size limit is defined by the signal-to-noise ratio. Small particles do not scatter much light, which leads to an insufficient measurement signal.

The basic setup of a DLS instrument is shown in Figure 16. A single frequency laser is directed to the sample contained in a cuvette. If there are particles in the sample, the incident laser light gets scattered in all directions. The scattered light is detected at a certain angle over time and this signal is used to determine the diffusion coefficient and the particle size by the Stokes-Einstein equation.

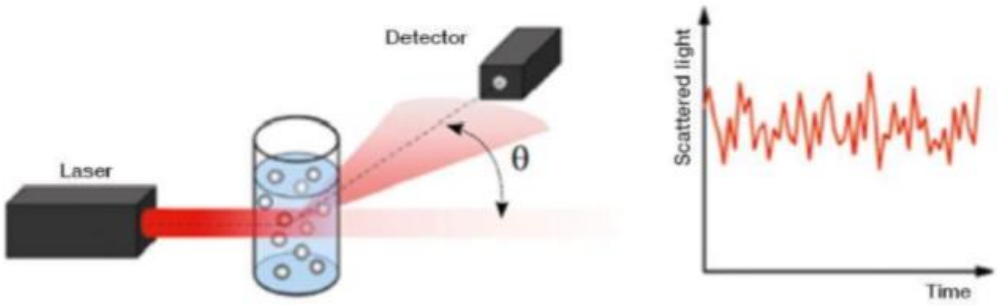

Figure 16. Basic setup of a DLS measurement system.[38] The sample is contained in a cuvette.

The scattered light of the incident laser can be detected at different angles. The incident laser light is usually attenuated by a gray filter which is placed between the laser and the cuvette. The filter settings are either automatically adjusted by the instrument or can be set manually by the user.

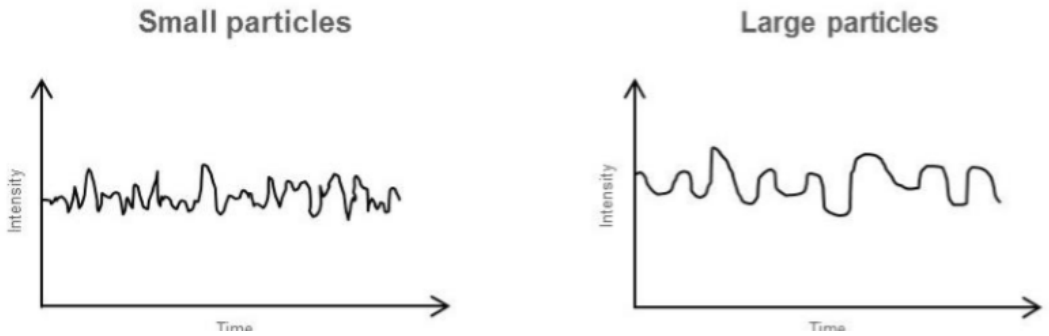

Figure 17. Differences in the intensity trace and correlation function of large and small particles.[38]

Smaller particles show faster fluctuations of the scattered light and a faster decay of the correlation function. When turbid samples are measured, the detector would not be able to process the number of photons. Therefore, the laser light is attenuated to receive a sufficient but processable signal at the detector.[38] The scattered light is detected over a certain time period in order to monitor the movement of the particles. The intensity of the scattered light is not constant but will fluctuate over time. Smaller particles, which are moving at higher speeds, show faster fluctuations than larger particles. On the other hand, larger particles result in higher amplitudes between the maximum and minimum scattering intensities, as shown in Figure 17. The polydispersity index (PDI) is given in order to describe the broadness of the particle size distribution. The polydispersity index is also calculated by the cumulant method. A value below 10 % reflects a monodisperse sample and indicates that all of the measured particles have almost the same size. Generally, the polydispersity index is considered good when it does not exceed the value of 30%. However, the polydispersity index does not provide any information about the shape of the size distribution or the ratio between two particle fractions.

2.3.4 UV-Vis Absorption. The absorption spectra of the aqueous CPNs were measured using a UV-VIS Analytik Jena AG Germany, Specord 205 spectrophotometer using a 1 cm path length quartz cuvette.

Figure 18. UV-VIS Analytik Jena AG Germany, Specord 205 spectrophotometer.

Optical spectroscopy is based on the Bohr-Einstein frequency relationship:

$\Delta E=E_2-E_1=h\ f$ (2.4.1)

This relationship links the discrete atomic or molecular energy states E_1 with the frequency

f of the electromagnetic radiation. The proportionality constant h is Planck's constant (6.626×10^{-34} J s). In spectroscopy, it is appropriate to use the wavelength v instead of frequency f. Equation (2.4.1) then takes the form:

$\Delta E=E_2-E_1=h\ c\ v$

where, $f= c/\lambda =c\ v$ (2.4.2)

The Bouguer-Lambert-Beer law forms the mathematical-physical basis of light-absorption measurements on gases and solutions in the UV-VIS and IR-region.[39,40]

Spectroscopic methods of chemical analysis, which include UV-Vis spectrophotometry, are widely used to solve various chemical problems related to structure, kinetics, identification and quantitative analysis of various compounds. In the visible spectroscopy study, a beam of radiation is directed to the test sample. The measurement of the radiation emitted by the sample is followed. Specifically, when measuring in quartz cuvettes (UV-VIS region) or cuvettes made of special optical glass (VIS region), part of the light is lost through reflection at the cuvette surfaces. In order to eliminate this source of

error, a reference measurement is made in a cuvette with the same path length but not containing the substance to be measured. Since most UV-VIS spectroscopy is carried out with solutions, the standard cuvette contains the pure solvent, which ideally should not absorb in the spectral region under consideration. In order to determine the absorbed radiation, we compare the intensity of the outflow beam from the cuvette to the sample containing the chemical species that absorb with the intensity of the beam coming out of the reference cuvette. The reference cuvette contains a blank sample that does not contain the test substance (or substance of interest). The intensity of the radiation emanating from the blank sample is considered to be the corrected intensity of the radiation incident to the sample. This intensity is practically equal to the actual intensity of the incident because the losses in the blank sample (due to scattering, reflection or absorption) are very small. Energy absorption requires a physical interaction between a photon and a particle of the chemical species that absorbs in the sample. The study of this absorption has led to the following equation:

$dI_a = -kI_a cddo$ (2.4.3)

where, k is a ratio constant, c is the concentration of the light-absorbing substance and d is the path length of the sample in cm. Io is the intensity of the monochromatic light entering the sample and I_δ is the intensity of this light emerging from the sample. The negative sign is introduced because the intensity, I, decreases as the absorption layer becomes thicker. After completion the above equation (2.4.3) gives:

$\log I_\delta / I_0 = -k\ dc$ /2,303 (2.4.4)

The fraction of the incident intensity exiting the sample defines the permeability, the latter equation is transformed as:

$\log T_0 = -\varepsilon_0 dc$ (2.4.5)

And also:

k /2,303= ε_0 (2.4.6)

$A_0 = -\log T_0$ (2.4.7)

where, ε_0 is the molar decadic extinction coefficient. The molar decadic extinction coefficient is a quantity characteristic of the substance which also depends on wavenumber v (cm^{-1}) or wavelength λ (nm). The functional correlation between ε_0 and

wavenumber v is called the “absorption spectrum” of a compound. Since the extinction coefficient can vary by several orders of magnitude within the absorption spectrum of a single inorganic or organic compound, the logarithmic value Iog ε_0 = f(v) can be used to plot an absorption spectrum. The Bouguer-Lambert-Beer law is a limiting law for dilute solutions, i.e. the assertion that the extinction coefficient is independent of the concentration of a substance at the given wavenumber (or wavelength) applies only to dilute solutions.

The equation that arises is:

$A_0 = -\varepsilon_0 dc$ (2.4.8)

The (2.4.8) equation is known as the Beer-Lambert law. The Beer-Lambert law assumes that the radiation is monochromatic, the chemical species they absorb display no interactions, the cross section of the sample is uniform, no fluorescence phenomena are observed and the concentrations in the active ingredients of the solutions from which the samples originate are small. It is very common to express the concentration of solutions in terms of percentages. The percentage concentration is calculated as the fraction of the weight or volume of the solute related to the total weight or volume of the solution. When the percentage concentration is calculated by weight, ε_0 is replaced by α_0 and the Beer-Lambert law is modified in the form bellow:

$A_0 = -adc_m$ (2.4.9)

where:

cm: is the concentration of the substance calculated in g L^{-1}

d: is the path-length of the sample (practically corresponds, as mentioned above, to the thickness of the cuvette usually 1 cm)

α: absorbance

The graph of the absorption relative to the concentration is linear.

3. Results and Discussion

3.1 Synthesis of Polymers

In this work, we focused on the synthesis of two chemically related conjugated polymers, both comprising of thiophene (Th) as the electron donating unit and quinoxaline (Q) as the electron withdrawing unit. The only variation between those two was the phenyl substitution for the IDTTDQ-Ph and the corresponding thiophene one for the IDTTDQ-Th. The scope is to investigate the correlation between structure, nanoparticle formation and optoelectronic properties. In Figures 19 and 20, a schematic representation of the synthesis is given. As shown in Figure 19, the reaction was left for 24h (IDTTDQ-Ph-HMW). In order to test how shorter reaction time would influence the molecular characteristics, the synthesis was repeated and left for 1h (IDTTDQ-Ph-LMW). For the synthesis of IDTTDQ-Th the reaction was terminated after 48h as shown.

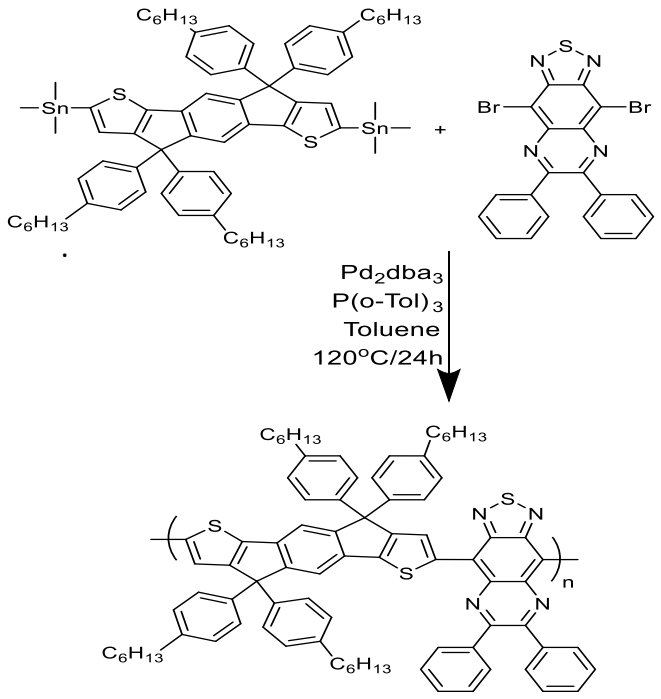

Figure 19. Schematic synthesis of IDTTDQ-Ph-HMW.

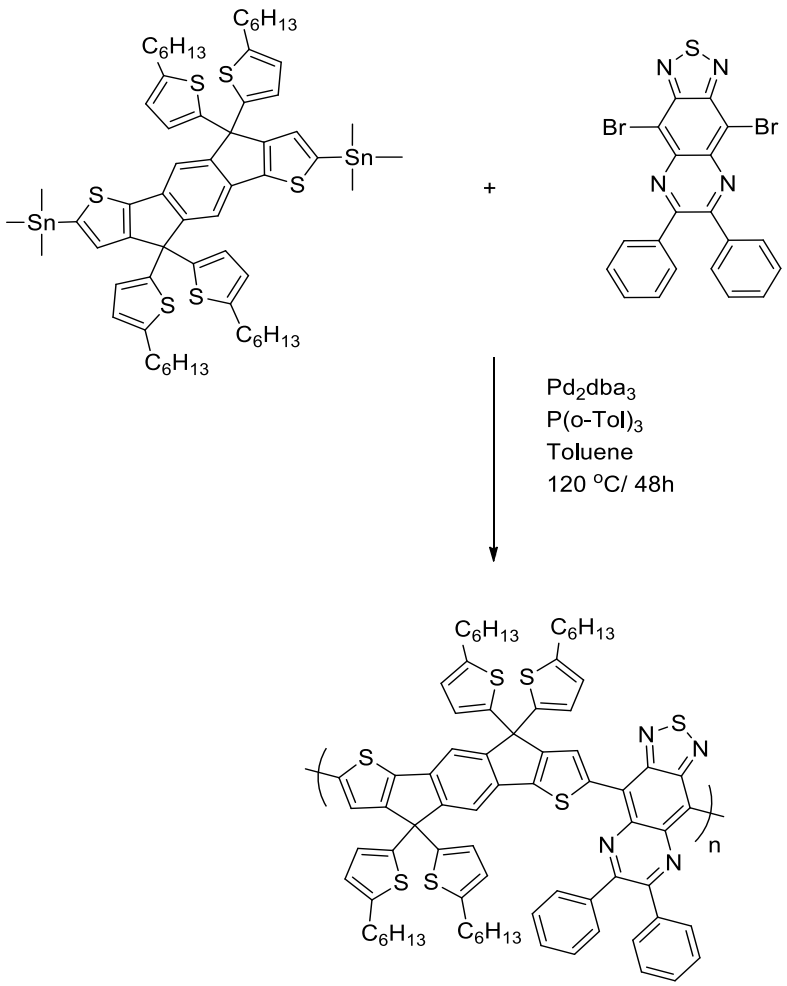

Figure 20. Schematic synthesis of IDTTDQ-Th.

Figure 21. The conjugated polymers, IDTTDQ-Th, IDTTDQ-Ph-LMW and IDTTDQ-Ph-HMW, in a row from left to right.

3.2 ^{1}H- Nuclear Magnetic Resonance

In figure 22 a and b, the ^{1}H-NMR spectra of the IDTTDQ-Ph and IDTTDQ-Th polymers in $CDCl_3$ (7.26ppm), are given. In both spectra the upfield region, between 0.85 to 2.76 ppm and 0.85 to 2.58ppm, for the IDTTDQ-Th and IDTTDQ-Ph, respectively, refers to the aliphatic protons. The aliphatic region in both spectra is similar as expected, since the only difference is that the final (-CH2-) group is connected in one case with a phenyl carbon (2.58ppm) and in the other with a thiophene carbon (2.76 ppm), so a slight left-shift is observerd for the IDTTDQ -Th. The rest aliphatic protons appear at 0.85ppm (12H) in both spectra, 1.27ppm, 1.36ppm (16H) and 1.61 ppm and 1.67 ppm (8H), respectively. As far as the aromatic protons are concerned, for the IDTTDQ-Th polymer, a total of 10H (6.62-6.95) ppm are expected for the thiophene rings , 10H(7.44-7.88) ppm are expected for the phenyl protons of the quinoxaline and the most deshielded are the 2H that appear at 9.31 ppm. For the IDTTDQ-Ph polymer, a total of 10H (8H+2H) (7.12) ppm are expected for the 4 phenyl rings and 2 thiophene rings, 18H (10H+ 8H) (7.35-7.58) ppm are expected for the rest phenyl protons and lastly the expected 2 phenyl protons (7.78ppm).

a

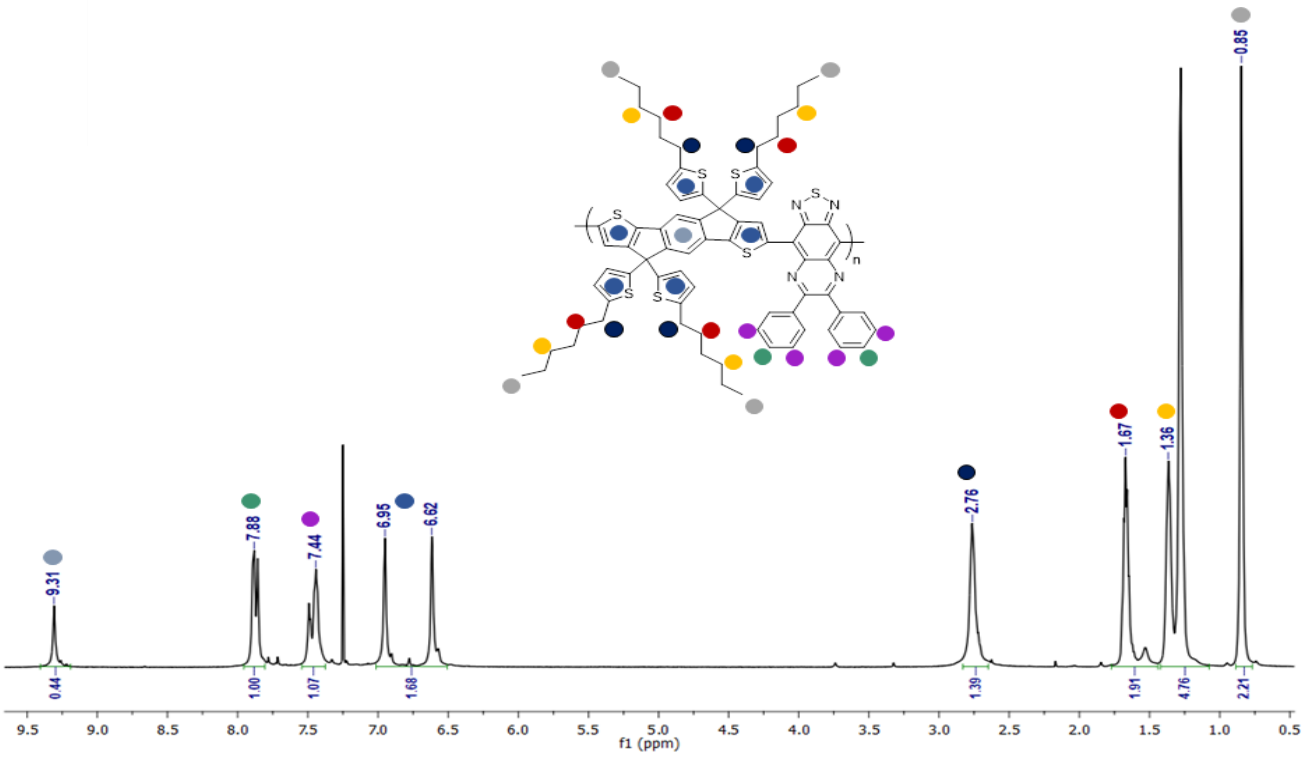

b

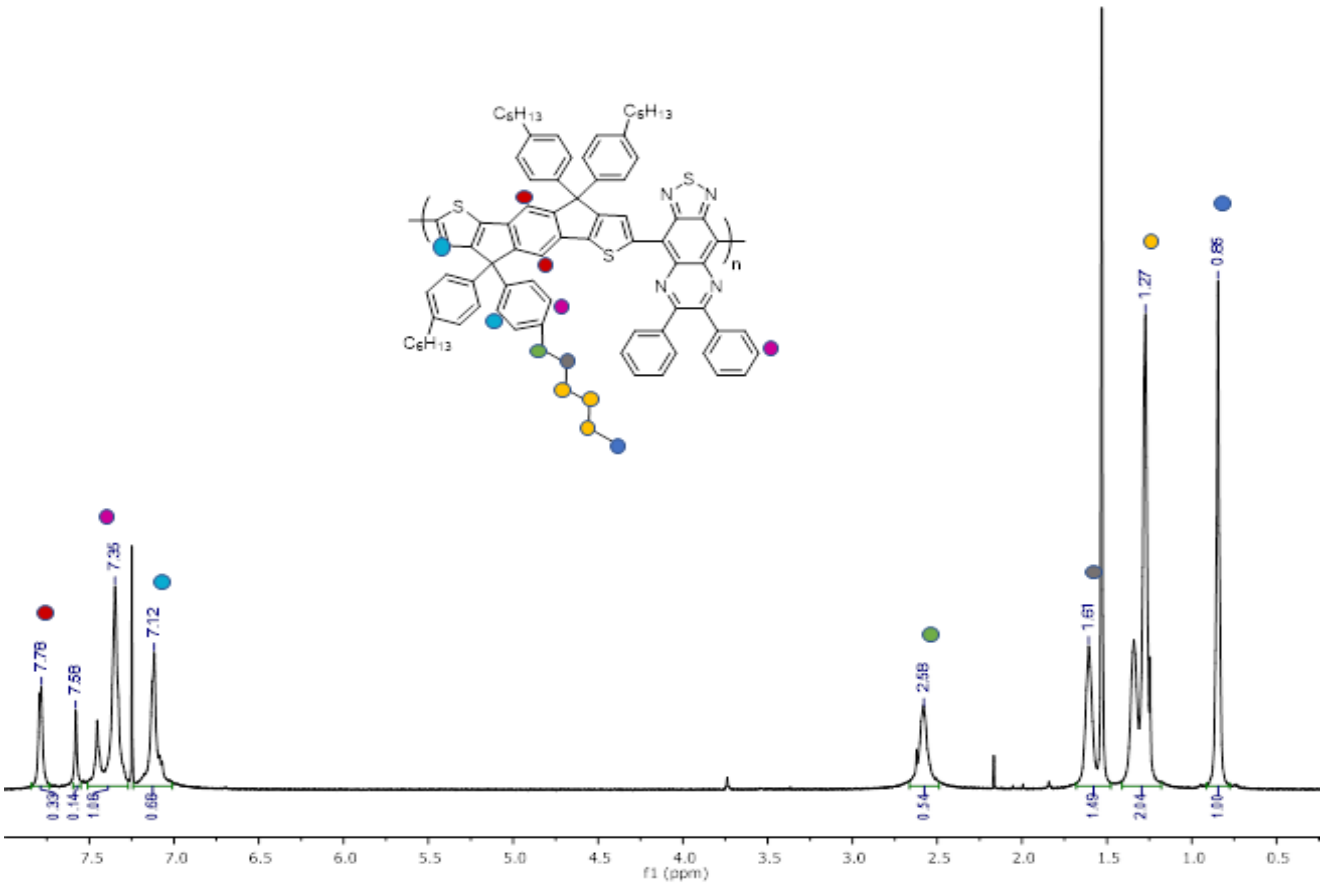

Figure 22 (a,b). ^{1}H-NMR spectra of IDTTDQ-Th and IDTTDQ-Ph polymers.

3.3 Gel Permeation Chromatography

From the acquired GPC graphs (Figure 22), we can observe that the IDTTDQ-Ph-HMW polymer reveal more than one distinct peaks (at least three). On the other hand, the IDTTDQ-Ph-LMW and the IDTTDQ-Th polymers, reveal at least two peaks. The average molecular weights per number ($\overline{M_n}$) and dispersity (Đ) of the chloroform-soluble fractions of the IDTTDQ-based polymers as measured by gel permeation chromatography (GPC) based on monodispersed polystyrene standards are summarized in Table 1. The dispersity index also verifies the more variable distribution of molecular weights of the IDTTDQ-Ph (Higher Molecular Weight), (6.3), in comparison to the dispersity index of both IDTTDQ-Ph (Lower Molecular Weight) and IDTTDQ-Th (3.5, 4.1 respectively).

Table 1. Molecular weight characteristics of the IDTTDQ based polymers.

Conjugated Polymers	$\overline{M}_n$ **(g mol^{-1})**	$\overline{M}_w$ **(g mol^{-1})**	***Đ***
IDTTDQ-Th	24.000	102.000	4.1
IDTTDQ-Ph(LMW)	28.000	99.000	3.5
IDTTDQ-Ph(HMW)	24.000	152.000	6.3

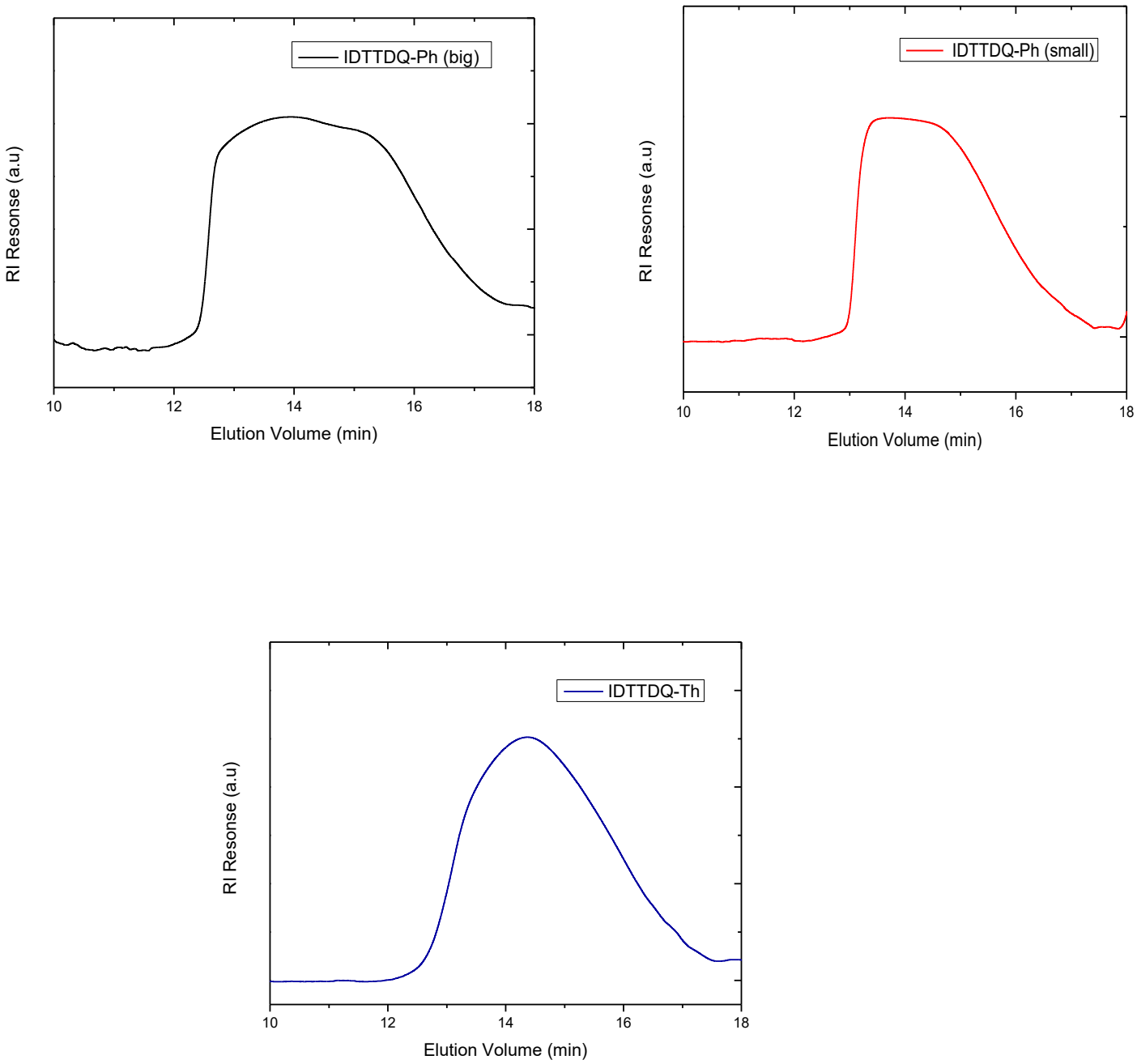

Figure 23. GPC chromatographs of the IDTTDQ-based conjugated polymers.

3.4 Preparation of nanoparticles

As it was thoroughly described in section 2.2.2, nanoparticles were mainly prepared with the encapsulation method. Tetrahydrofuran (THF), was chosen as the solvent for the CP-*m*PEG-*b*-PLGA solution, owing to the fact that it is a low boiling point, aprotic polar solvent, miscible with water. Plus, the choice of *m*PEG-*b*-PLGA was based on the fact that it is an FDA approved and metabolizable copolymer.[34] By applying the encapsulation method, the hydrophobic PLGA segments are liable to entangle with the hydrophobic polymer chains and the hydrophilic PEG chains should extend into the aqueous phase. As it is shown in Figure 24, the mixing between the *m*PEG-*b*-PLGA and each conjugated polymer, under sonication in water, leads to a yellow solution. Different blending ratios result in slight color differences. Generally, a more intense yellow color is expected with increasing polymer solution added in water.

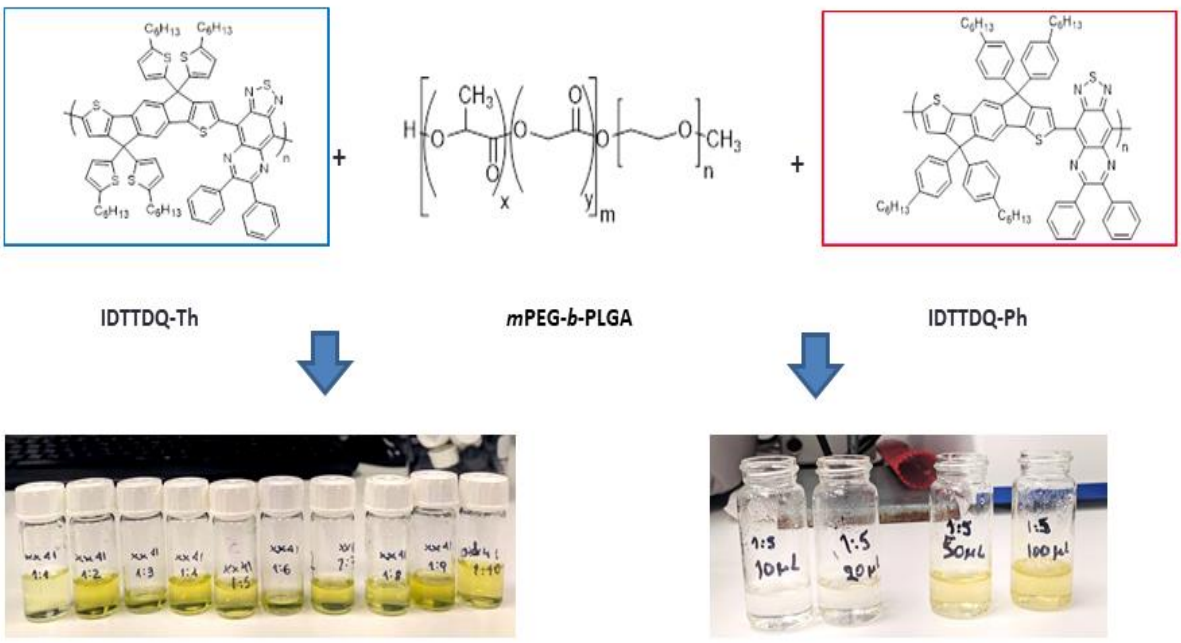

Figure 24. Representation of encapsulation approach for the IDTTDQ-Th and IDTTDQ-Ph-LMW polymers.

The objective, is to find the optimum blending ratio which would lead to the maximum photoacoustic signal. In figure 24, a representation of the blending process is shown for the IDTTDQ-Th polymer, in all mixing ratios with *m*PEG-*b*-PLGA, using 1ml of each CP-*m*PEG-*b*-PLGA solution. On the other hand, different quantities of each IDTTDQ-Ph-LMW-*m*PEG-*b*-PLGA solution were examined, less than 1 ml. This was attributed to the higher hydrophobicity of the IDTTDQ-Ph-LMW polymer in contradiction to the IDTTDQ-Th polymer, which led to the almost instant formation of aggregates when in contact with water. As expected, the formation of IDTTDQ-Ph-HMW nanoparticles is even more hindered due to the even higher hydrophobicity of the polymer so from now on, all measurements will be referring to the IDTTDQ-Ph-LMW nanoparticles as IDTTDQ-Ph nanoparticles.

3.5 DLS and Zeta Potential

As it was previously mentioned, CP nanoparticles were prepared with the encapsulation and the nanoprecipitation method. To evaluate the sizes of the formatted aqueous IDTTDQ-based polymer nanoparticles, dynamic light scattering (DLS) measurements were performed at room temperature, 25^{o}C, a day after their preparation and the results are depicted in Tables 2, 3, 4. The encapsulated IDTTDQ-Th CPNs exhibit a hydrodynamic diameter between 108,73 ± 0,20 nm and 120,10 ± 0,29 nm.

Table 2. DLS and Z potential measurements of the encapsulated IDTTDQ-Th nanoparticles.

Sample IDTTDQTh: Amph	DLS Athens (25^{o}C)				
	Z-Ave (nm)	PDI	PK1 mean(nm)	Z potential	Std dev
1:1	113,90± 0,32	0,144 ± 0,016	130,93 ± 1,88	-17,7	18,3
1:2	112,10 ± 0,17	0,158 ± 0,009	135,70 ± 1,65	-19,6	10,4
1:3	116,53 ± 0,28	0,171 ± 0,004	143,53 ± 1,46	-18,0	9,41
1:4	120,10 ± 0,29	0,176 ± 0,012	149,50± 2,53	-16,5	7,64
1:5	108,73 ± 0,29	0,21 ± 0,002	139,63 ± 1,62	-17,2	8,22
1:6	110,97 ± 1,29	0,218 ± 0,008	151,80 ±4,56	-13,9	9,4
1:7	109,73 ± 0,67	0,198 ± 0,003	134,47 ± 2,10	-17,4	8,34
1:8	109,23 ± 0,39	0,201 ± 0,002	139,70 ± 0,17	-12,3	6,72
1:9	116,93 ± 0,12	0,194 ± 0,006	148,37 ± 2,18	-16,9	7,73
1:10	118,50 ± 0,36	0,225 ± 0,003	159,50 ± 3,91	-19,5	5,49

Moreover, the distribution of nanoparticle sizes, demonstrate a unimodal size distribution (Figure 25) with low polydispersity indexes (PDIs), between 0,144 ± 0,016 and 0,225 ± 0,003 for all the IDTTDQ-Th NPs (Table 2)**.** Simultaneously with the DLS measurements, the zeta potential of the CPNs was measured. The corresponding ones prepared via the encapsulation method exhibit a zeta potential ranging between -12,3 to -19,6 mV. It is well known that stable polymer nanoparticles in water adopt a micellar structure consisting of a hydrophobic core and a hydrophilic shell. However, on the basis of their chemical structures, the conjugated polymers used in this study would exhibit strictly hydrophobic characteristics. Therefore, we hypothesize that chemical modifications of the conjugated polymer during the nanoparticle formation lead to hydrophilic defects[44, 45] Consequently, the origin of the negative zeta potential is attributed to oxidative defects on the surface of the CPNs or to the presence of the p-polarizations of the polymer rings that enable stronger attractive van der Waals forces and hydrophobic interactions. Therefore, when the conjugated polymer is encapsulated inside the amphiphilic copolymer, those interactions are minimized resulting in lower zeta potential values in comparison with the coresponding nanoprecipitated nanoparticles, as shown in Table 4.[31]

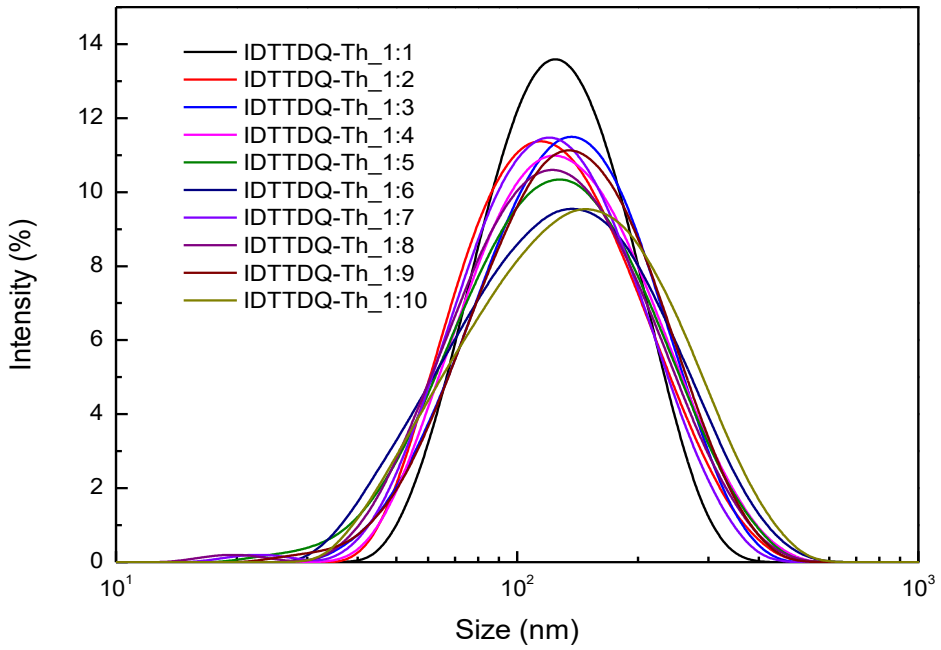

Figure 25. Particle size distribution of IDTTDQ-Th nanoparticles: CP:*m*PEG-b-PLGA (1mg: 1-10mg), centrifuged 5min, 1000rpm, filtered, 25°C.

As it results from Table 3, the PDI for the encapsulated IDTTDQ-Ph NPs is the highest (0,317 ± 0,039) for the 1:1 mixing ratio and 100μl while the preferable PDIs (0,158 ± 0,002 and 0,168 ± 0,003), appear for the mixing ratios 1:5, 1:6 and 1:9 and the largest quantity (700μl), (Figure 26). It should be mentioned that a larger quantity was not added, due to the high hydrophobicity of the polymer and the formation of aggregates.

Table 3. DLS and z potential measurements of the IDTTDQ-Ph encapsulated nanoparticles.

Sample IDTTDQPh: Amp	DLS Athens (25 °C)				
	Z-Ave (nm)	PDI	PK1 mean(nm)	Z potential	Std dev
1:1 100μl	125,13 ± 7,03	0,317 ± 0,039	171,6 ± 14,26	-18,9	20,1
1:1 700μl	96,29 ± 0,53	0,217 ± 0,003	127,5 ± 2,66	-21,6	10,5
1:2 200μl	80,31 ± 0,48	0,229 ± 0,007	76,83 ± 32,57	-20,5	9,27
1:6 700μl	84,26 ± 0,12	0,158 ± 0,002	99,95 ± 1,03	-21,7	9,35
1:5 20μl	116,3 ± 2,91	0,26 ± 0,019	146,73 ± 8,44	-26,1	42,2
1:5 50μl	84,96 ± 0,36	0,194 ± 0,008	106,83 ± 1,13	-18,7	10,6
1:5 100μl	87,43 ± 0,41	0,211 ± 0,006	115,03 ± 1,99	-18,9	20,1
1:5 700μl	86,39 ± 0,12	0,168 ± 0,003	103,63 ± 3,58	-18,2	12,4
1:9 10μl	100,8 ± 1,05	0,18 ± 0,006	125,3 ± 1,68	-20,9	12,7
1:9 20μl	99,59 ± 0,41	0,169 ± 0,004	119,10 ± 2,84	-19,33	23,9
1:9 50μl	94,49 ± 0,29	0,206 ± 0,009	119,07 ± 1,57	-20,7	10,3
1:9 100μl	93,89 ± 0,55	0,169 ± 0,007	115,43 ± 1,29	-20,7	22,1
1:9 700μl	85,33 ± 0,12	0,163 ± 0,004	101,60 ± 1,35	-18,2	10,4

In addition, these encapsulated CPNs indicate a size distribution dependent on the various mixing ratios of the polymers and also the final solution quantity injected in water. More specifically, the mixing ratios 1:5, 1:6 and 1:9 show a more uniform distribution than the 1:1 and moreover the 700μl of solution injected in water, show a more narrow distribution in all mixing ratios. The IDTTDQ-Ph NPs exhibit a zeta potential ranging between and -18,2 to -26,1 m V.

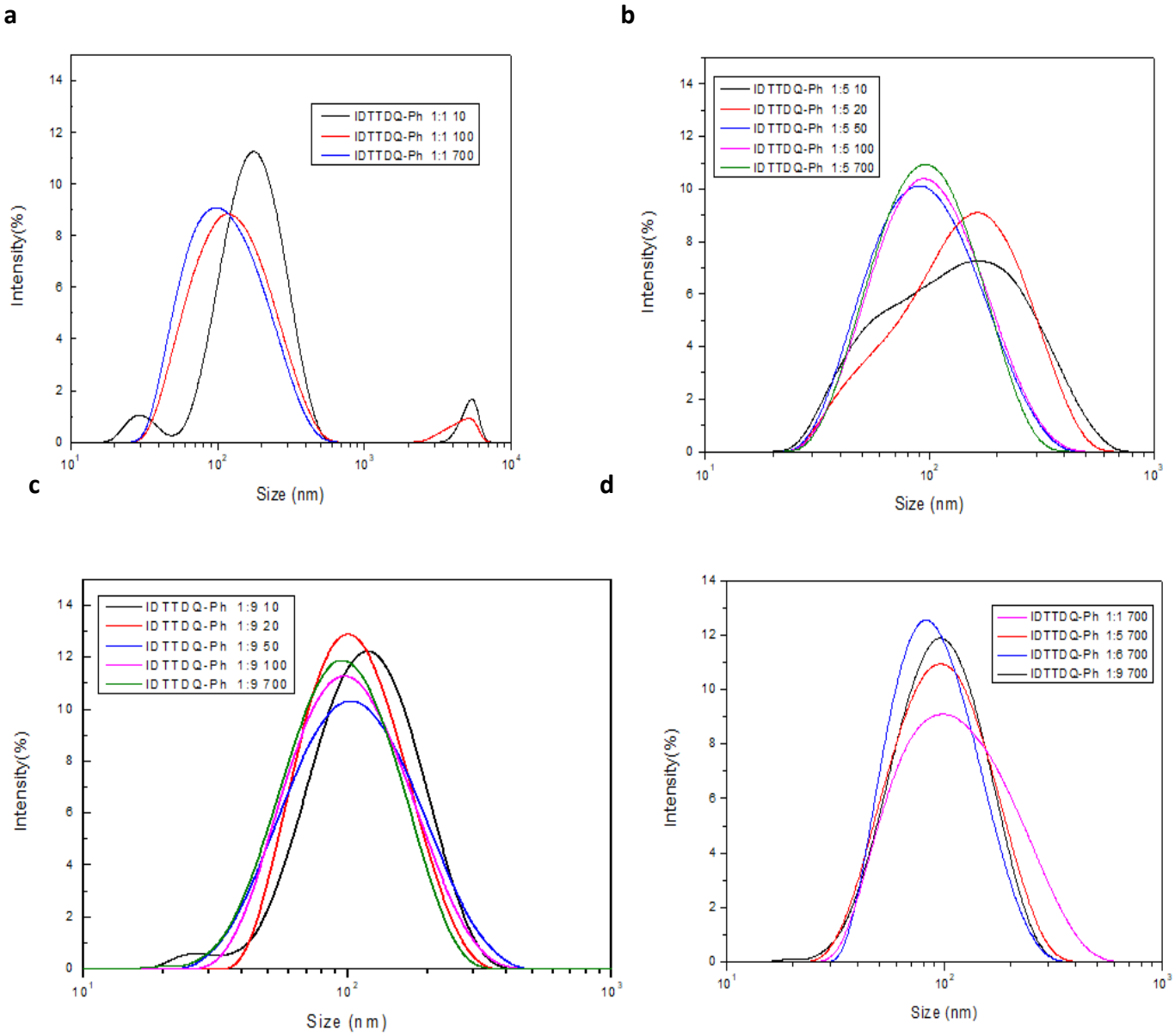

Figure 26. Particle size distribution of IDTTDQ-Ph-LMW nanoparticles centrifuged 5min, 1000rpm, filtered, 25°C. a. [CP:Amph= 1mg: 1mg, 10, 100, 700 μl], **b**. [CP: Amph= 1mg:5mg, 10, 20, 50, 100, 700 μl] **c**. [CP: Amph= 1mg:9mg, 10, 20, 50, 100, 700 μl], **d**. [700μl (CP: Amph)= (1mg: 1, 5, 6, 9)mg].

The nanoprecipitated IDTTDQ-Th NPs exhibit a hydrodynamic diameter of 76,43 ± 0,57nm which is smaller than the encapsulated ones. This size difference originates from the use of the *m*PEG-b-PLGA block copolymer. Plus, they exhibit a PDI of 0.208 ± 0.005. The formation of nanoparticles using the nanoprecipitation method is a surfactant-free approach and the colloidal stability arises from the inherent surface characteristics of the conjugated polymer NPs. The resistance of low-bandgap CP NPs to undergo aggregation in water is attributed to the substantial and negative zeta potential (-24,5 mV)discussed above and it is shown in Table 4.

Table 4. DLS and z potential measurements of the IDTTDQ-Ph-LMW and IDTTDQ-Ph nanoprecipitated nanoparticles.

Sample	DLS Athens (25 °C)				
	Z-Ave (nm)	PDI	PK1 mean(nm)	Z potential	Std dev
IDTTDQTh-NANP (600µl)	76,43 ± 0,57	0.208 ± 0,005	83,78 ± 1,22	-24,5	7,19
IDTTDQPh-NANP (2ml)	95,61 ± 0,38	0,305 ± 0,024	154,33 ± 22,98	-22	15,5

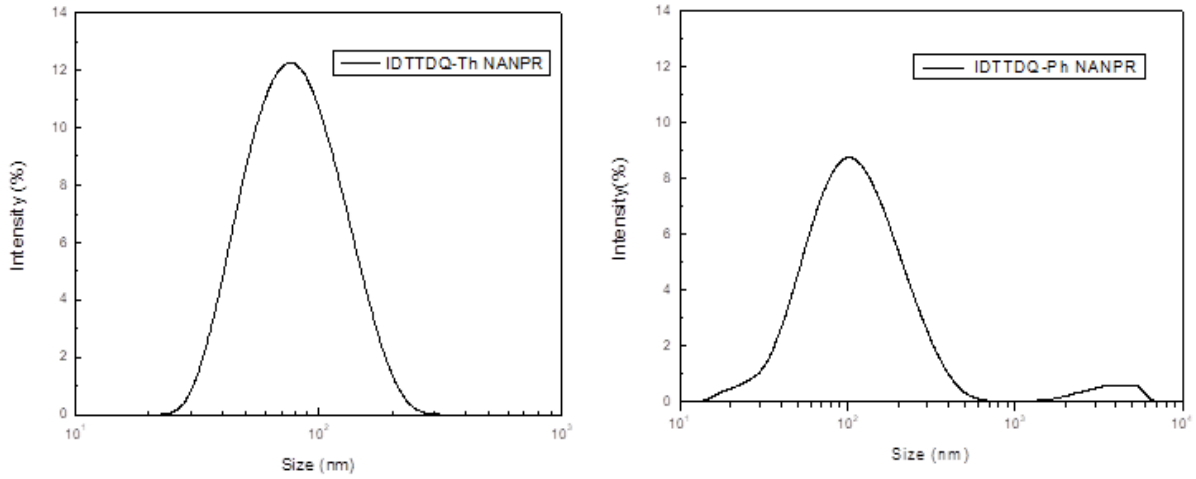

Figure 27. Particle size distribution of IDTTQ-Ph and IDTTDQ-Th nanoprecipitated nanoparticles, filtered, 25°C.

The nanoprecipitated IDTTDQ-Ph nanoparticles in this case do not show a unimodal distribution which is also depicted in their PDI (0,305 ± 0,024), in Table 4 and show a negative zeta potential of -22 mV**.** It is well known that colloidal suspensions systems with a zeta potential value of –25 mV or lower maintain a long-term colloidal stability.[42,43] Finally, in all cases, the average particle size was around 100 nm, which is an acceptable size for biological applications. Furthermore, according to previous studies the dimensions and the shape of the NPs are critical factors in order for the CPNs to escape the endothelium. NPs >200 nm are cleared in the liver and spleen, while <10 nm are cleared from the kidneys. The optimal size for the NPs is considered to be between 10nm and 200 nm. [46]

3.6 UV-Vis Spectroscopy

Based on the UV-Vis spectrum (Figure 28), IDTTDQ-Th nanoparticles absorb in the visible region around 450nm and in the NIR-II region around 1000nm. The highest absorbance arises from the blending ratio, 1mg: 9mg (conjugated polymer: amphiphilic polymer) and the lowest from the 1mg: 1mg respectively. However, almost all blending ratios (1:4-1:10) seem to absorb as well.

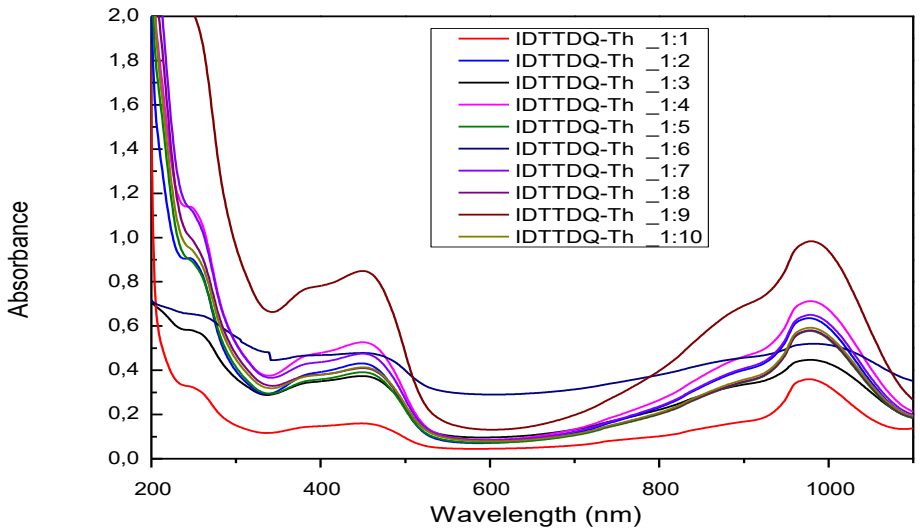

Figure 28. UV-Vis absorption spectra of the low-bandgap IDTTDQ-Th. [CP:Amph=1mg:1-10mg], (centrifuging 5min, 1000rpm).

For each polymer, two major absorption bands are observed in solution, a phenomenon commonly observed for Donnor–Acceptor copolymers. The absorption at the lower wavelengths can be attributed to π–π* transitions while the high-wavelength peak is related to an intramolecular Donor–Acceptor charge transfer.[41] As shown in Figure 29 below, the maximum absorbance of all the IDTTDQ-Ph nanoparticles is around 1000nm and the previous demonstrated absorbance in the visible region is barely existent. Consequently, the most promising blending ratio in this case is the [CP: Amph=1mg: 9mg] and 700 μl of solution, where the polymer seems to be partially encapsulated.

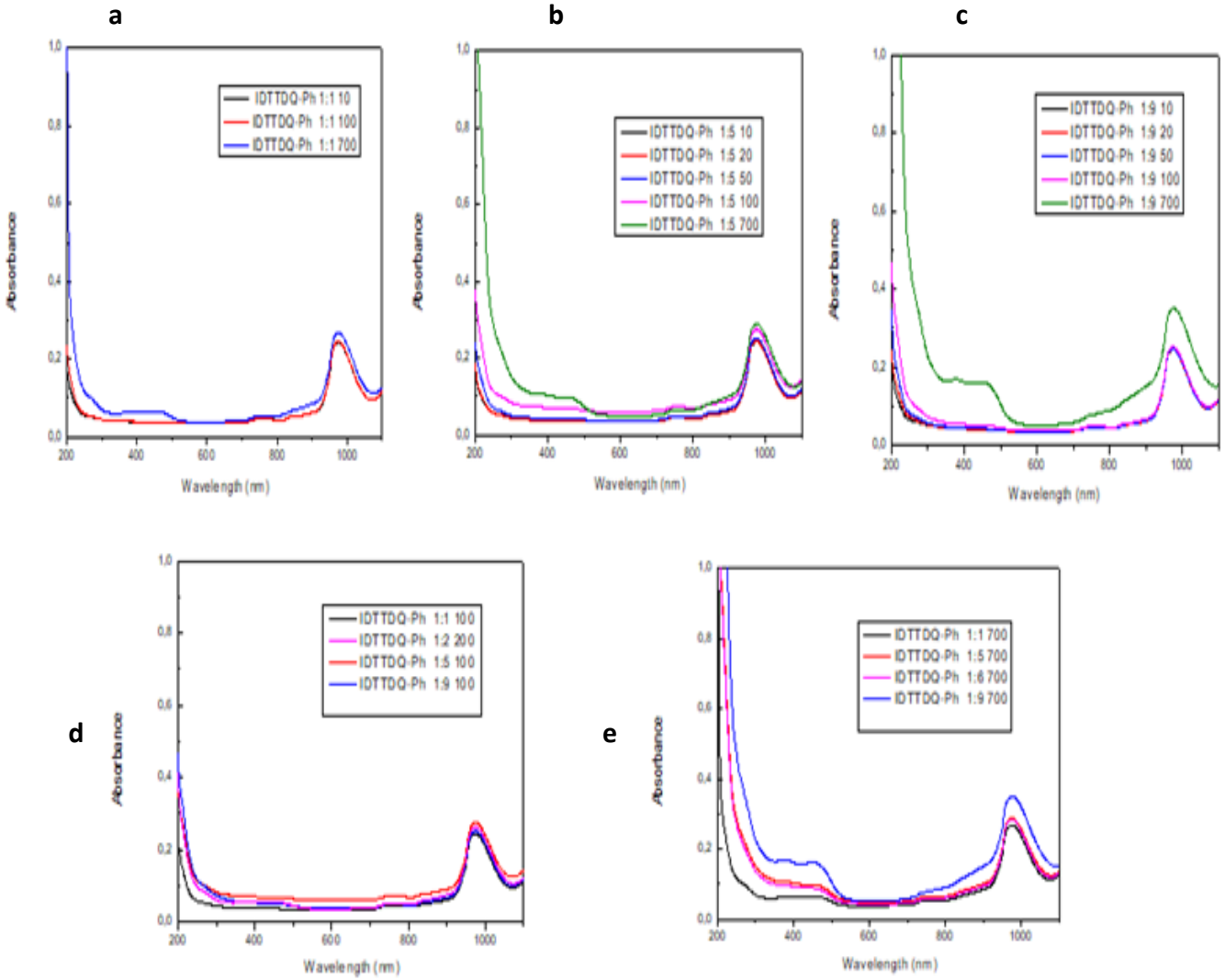

Figure 29. UV-Vis absorption spectra of the low-bandgap IDTTDQ-Ph.

a. [(CP: Amph)= (1mg: 1mg), 10, 100, 700 µl]], **b**. [(CP: Amph)= (1mg: 5mg), 10, 20, 50, 100, 700 µl], **c**. [(CP: Amph)= (1mg:9mg), 10, 20, 50, 100, 700 µl], **d**. [(CP: Amph= 1mg: 1,5,9 mg) 100µl, (CP: Amph= 1mg: 2mg) 200µl], **e**. [700µl (CP: Amph= 1mg: 1, 5, 6, 9 mg)].

The same behavior is observed for both the nanoprecipitated IDTTDQ-Ph and IDTTDQ-Th nanoparticles (Figure 30) and it should be pointed out that neither the nanoprecipitated forms nor the encapsulated IDTTDQ-Ph nanopartcles absorb as stongly as the encapsulated IDTTDQ-Th NPs.

It is well known, that the NIR-II (1,000–1,700 nm) absorption leads to deeper tissue optical imaging as a result of further reduced scattering, and tissue absorption when in comparison with the absorption in the visible region of the spectrum.[6]

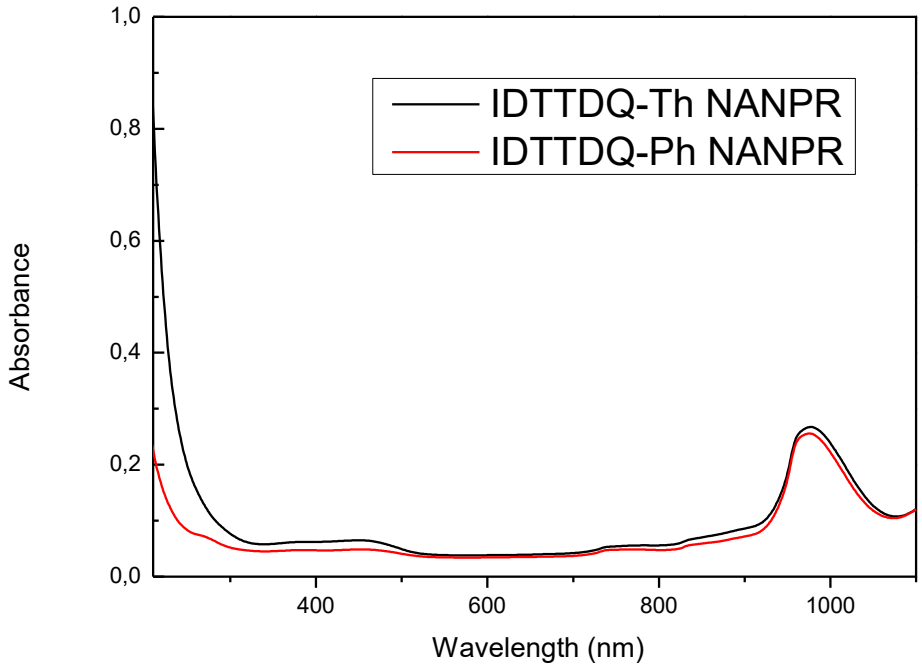

Figure 30. UV-Vis absorption spectra of the low-bandgap IDTTDQ-Ph and IDTTDQ-Th nanoprecipitated nanoparticles.

3.7 Photoacoustic Imaging

The photoacoustic imaging was performed at the German Cancer Research Center (DKFZ), using a Fujifilm, Vevo3100, lazer 970nm (Figure 31). The experiment was carried out with Phantom testing. As it is shown in Figure 32, the capillary tubes were filled with the sample and the rest space is covered with water. Then, the phantom is placed onto the instrument, the transducer is adjusted at the right height for the sample and the measurement begins.[47]

Figure 31. Fujifilm, Vevo3100, lazer 970nm.

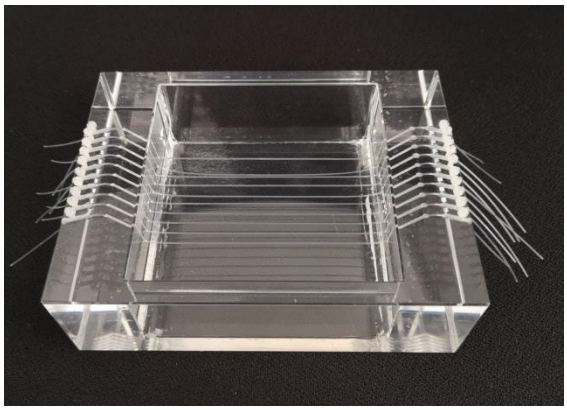

Figure 32. Phantom test.

In Figure 33, the photoacoustic spectra of the encapsulated IDTTDQ-Th, [CP: *m*PEG-b-PLGA (1mg: 9mg)] and IDTTDQ-Ph nanoparticles is recorded, by measuring the sound at different wavelengths of the light (680nm- 970nm)**.** A higher intensity in the NIR-I region (around 900nm), is observed for the encapsulated IDTTDQ-Th CPNs in comparison with the IDTTDQ-Ph CPNs where only the background noise is recorded (water). This is in agreement with the previously analyzed UV-Vis spectra showing the most prominent absorbance of this specific IDTTDQ-Th CPNs.

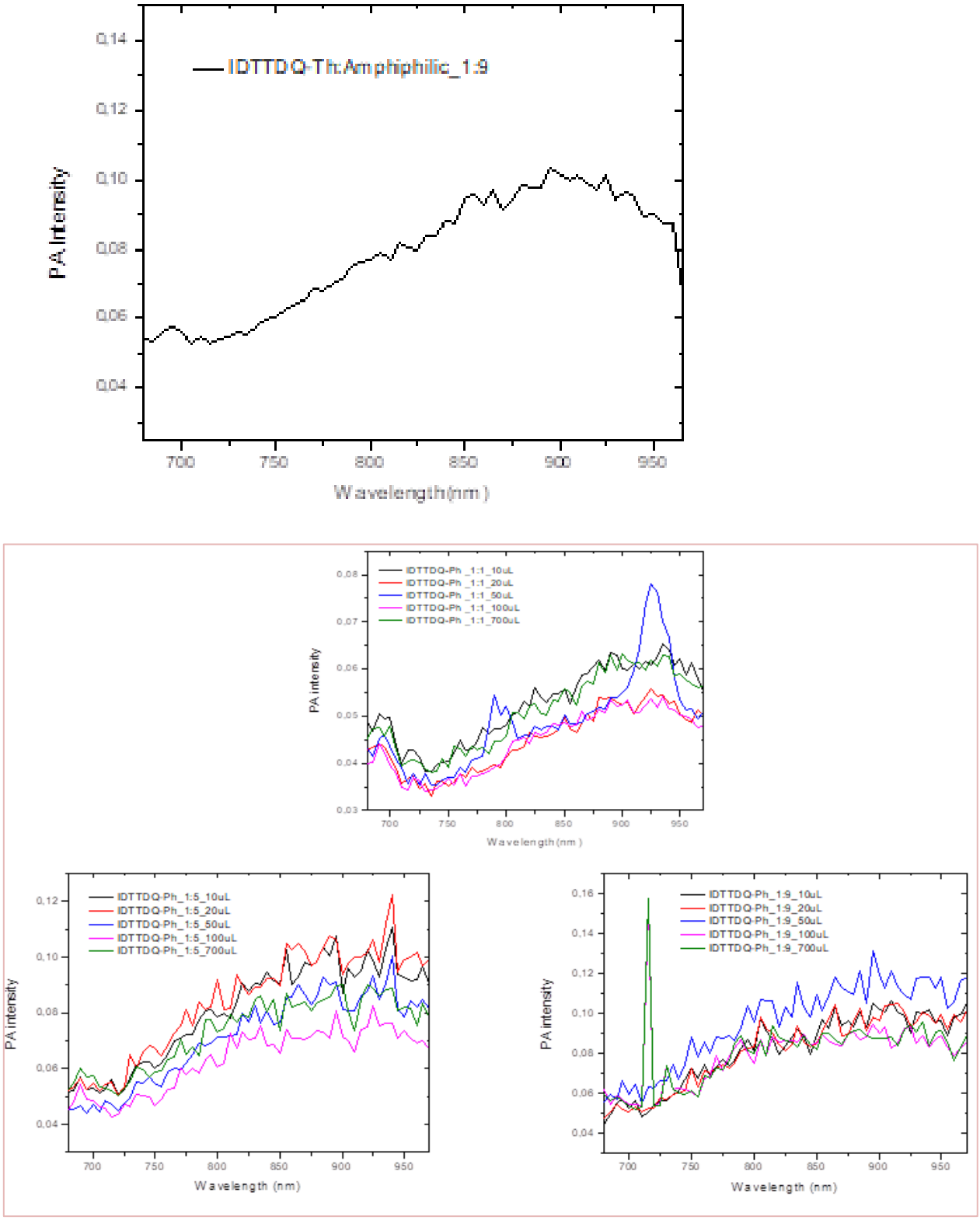

Figure 33. The photoacoustic spectrum of the encapsulated IDTTDQ-Th, [CP:*m*PEG-b-PLGA (1mg: 9mg)] **and IDTTDQ-Ph nananoparticles.**

4. Conclusions

Advancements in the fields of technology, energy and healthcare are directly related t o the evolution of the human species and its quality of life. To this end, new methods and materials for energy generation and saving as well as early diagnosis of diseases and more effective therapeutic approaches, using more efficient ways, are indispensable. Among them, nanoparticles based on conjugated polymers are emerging as multifunctional nanoscale materials that have been developed as candidates with great potential to offer in these areas. Conjugated polymer nanoparticles (CPNs) are desirable for a number of reasons, which include charge carrier transport, tuneable optical properties and bright fluorescence with good photostability and large Stokes shifts. The fact that they are organic materials has also boosted the interest in their biological application, which has been evidenced in the recent efforts to produce biodegradable conjugated polymers. Besides being used for bioimaging, CPNs have also been studied as drug delivery systems for hydrophobic drugs (eg. Doxorubicin), including photoresponsive drug release, biosensors and as theranostic agents for cancer treatment. Moreover, their optoelectronic properties can be exploited and fine-tuned in the field of bioimaging, by appropriate molecular design and thus result in the desired absorption shift from the visible to the advantageous NIR region of the spectrum. In that way, fluorescence and photoacoustic biomaging are gaining more and more ground. Focusing on the photoacoustic bioimaging, the image acquisition by photoacoustic imaging takes advantage of the variable tissue distribution of endogenous light absorbing components, and their particular light absorbance characteristics. Accordingly, the technique can distinguish anatomical features while also providing physiological information and exogenous agents like conjugated polymer nanoparticles can successfully provide high resolution and deep penetration imaging in real time.

In this thesis, the IDTTDQ-Ph and IDTTDQ-Th conjugated polymers were successfully synthesized and characterized, by combining thiophene as the electron donating and quinoxaline as the electron deficient component of the polymer leading to low band-gap conjugated polymers. In addition, the spectral and colloidal properties of the IDTTDQ-Ph

and IDTTDQ-Th conjugated polymer nanoparticles, prepared with the encapsulation and the nanoprecipitation method, are reported. These CPNs exhibit colloidal stability owing to a negatively charged surface, with a zeta potential ranging between -12,3 to -26,1mV. Furthermore, as determined using DLS, the IDTTDQ-Th CPNs exhibit a unimodal size distribution and a hydrodynamic diameter around 100 nm, acceptable for biological applications. On top of that, the low-bandgap CPNs exhibit absorption in the NIR II window (1000 nm) paving the way for in vivo photoacoustic imaging. Finally the photoacoustic signal of the IDTTDQ-Th and IDTTDQ-Ph nanoparticles was recorded, showing promising results for NIR-I imaging, using the IDTTDQ-Th CPNs, as it was already expected, based on the UV-VIS absorption spectra. After attaining an optimized photoacoustic signal and testing their long term stability and reproducibility, In vitro cytotoxity testing in cancer cells would be the next step as well as testing their photothermal properties. The synthesis of a targeted multifunctional theranostic agent, providing imaging and phototherapy non-invasively would be the ultimate goal. Nevertheless, several challenges need to be addressed such as their in vitro biocompatibility assessment, systemic toxicity and the possible interactions of the light-induced charge transfer with other biological activities.

.

5. References

[1]. Fass, L. (2008). Imaging and cancer: A review. Molecular Oncology, 2(2), 115–152. doi:10.1016/j.molonc.2008.04.001

[2]. Guosong Hong, Alexander L. Antaris, Hongjie Dai(2017). Near-infrared fluorophores for biomedical imaging. Nature Biomedical Engineering 1(1):0010
DOI: 10.1038/s41551-016-0010

[3]. Siegel, R. L., Miller, K. D., & Jemal, A. (2019). Cancer statistics, 2019. CA: A Cancer Journal for Clinicians*, 69(1), 7–34.* doi:10.3322/caac.21551

[4]. Hawkes, N. (2019). Cancer survival data emphasise importance of early diagnosis. *BMJ, l408.* doi:10.1136/bmj.l408

[5]. Anne Hellebust and Rebecca Richards-Kortum. (2012). Advances in molecular imaging: targeted optical contrast agents for cancer diagnostics, Nanomedicine (Lond). 2012 Mar; 7(3): 429–445., doi:10.2217/nnm.12.12.

[6] Chulhong Kim, Ruogu Qin, Jeff S. Xu, Lihong V. Wang, Ronald X. Xu J. (2010). Multifunctional microbubbles and nanobubbles for photoacoustic and ultrasound imaging of Biomedical Optics. 15(1), 010510. doi: https://doi.org/10.1117/1.3302808

[7] Kai Cheng, Zhen Cheng. (2012) Diagnostic Applications. Adverse Effects of Engineered Nanomaterials
DOI: 10.1016/B978-0-12-386940-1.00015-5

[8]. Seung Hee Han. (2018). Review of Photoacoustic Imaging for Imaging-Guided Spinal Surgery. Neurospine 2018; 15(4): 306-322.
doi: https://doi.org/10.14245/ns.1836206.103

[9] Jeevanandam, J., Barhoum, A., Chan, Y. S., Dufresne, A., & Danquah, M. K. (2018). Review on nanoparticles and nanostructured materials: history, sources, toxicity and regulations. Beilstein Journal of Nanotechnology, 9, 1050–1074. doi:10.3762/bjnano.9.98

[10]. Fedatto Abelha, T., Dreiss, C. A., Green, M., & Dailey, L. A. (2020). Conjugated polymers as nanoparticle probes for fluorescence and photoacoustic imaging. Journal of Materials Chemistry B. doi:10.1039/c9tb02582k

[11]Harun, M.H.; Saion, E.; Kassim, A.; Yahya, N.; Mahmud, E. Conjugated conducting polymers: A brief overview. UCSI Acad. J. J. Adv. Sci. Arts 2007, 2, 63–68.

[12]K. Li and B. Liu, Polymer Encapsulated Conjugated Polymer Nanoparticles for Fluorescence Bioimaging, J. Mater. Chem., 2012, 22, 1257. 22 C.

Guenes, S., Neugebauer, H., & Sariciftci, N. S. (2007). Conjugated Polymer-Based Organic Solar Cells. ChemInform, 38(31). doi:10.1002/chin.200731220

[13]. Huo, L., Chen, H.-Y., Hou, J., Chen, T. L. &Yang, Y. Low band gap dithieno[3,2-b:2 ‘,3 ‘-d]silole-containing polymers, synthesis, characterization and photovoltaic application. Chem. Commun. 5570-5572 (2009).

[14]. Pavase, T. R., Lin, H., Shaikh, Q., Hussain, S., Li, Z., Ahmed, I., Kalhoro, M. T. (2018). Recent advances of conjugated polymer (CP) nanocomposite-based chemical sensors and their applications in food spoilage detection: A comprehensive review. Sensors and Actuators B: Chemical, 273, 1113–1138.doi:10.1016/j.snb.2018.06.118.

[15]. https://www.nobelprize.org/uploads/2018/06/heeger-lecture.pdf

[16] Yang, G., Phua, S. Z. F., Bindra, A. K., & Zhao, Y. (2019). Degradability and Clearance of Inorganic Nanoparticles for Biomedical Applications. Advanced Materials, 1805730. doi:10.1002/adma

[17]. Choi, S.-J., Lee, J. K., Jeong, J., & Choy, J.-H. (2013). Toxicity evaluation of inorganic nanoparticles: considerations and challenges. Molecular & Cellular Toxicology, 9(3), 205–210. doi:10.1007/s13273-013-0026-z

[18] V. Rohatgi, Low-Bandgap Conjugated Polymer Dots for Near-Infrared Fluorescence Imaging., ACS Appl. Nano Mater., 2018, 1 (9), pp 4801–4808 DOI: 10.1021/acsanm.8b01014

[19]. Zhu, C.; Liu, L.; Yang, Q.; Lv, F.; Wang, S. Water-Soluble Conjugated Polymers for Imaging, Diagnosis, and Therapy. Chem. Rev. 2012, 112, 4687-4735

[20]. Feng, L., Zhu, C., Yuan, H., Liu, L., Lv, F., & Wang, S. (2013). Conjugated polymer nanoparticles: preparation, properties, functionalization and biological applications. Chemical Society Reviews, 42(16), 6620.doi:10.1039/c3cs60036j

.201805730

[21] Wu, C. & Chiu, D. T. Highly fluorescent semiconducting polymer dots for biology and medicine. Angew. Chem. Int. Ed. 52, 3086–3109 (2013).

[22] W. Locke and the ICSTM Department of Chemistry 1996-97.

[23] Qian, C., Chen, Y., Feng, P., Xiao, X., Dong, M., Yu, J., Gu, Z. (2017). Conjugated polymer nanomaterials for theranostics. Acta Pharmacologica Sinica, 38(6), 764–781. doi:10.1038/aps.2017.42

[24] Hashemi, D., Ma, X., Ansari, R., Kim, J., & Kieffer, J. (2019). Design principles for the energy level tuning in donor/acceptor conjugated polymers. Physical Chemistry Chemical Physics, 21(2), 789–799. doi:10.1039/c

[25] Encyclopedia of Polymeric Nanomaterials DOI 10.1007/978-3-642-36199-9_5-1

[26] Davies, A. M. C. (2005). An Introduction to near Infrared Spectroscopy. NIR News, 16(7), 9–11. doi:10.1255/nirn.853.

[27] Miyaura, N. and Suzuki, A. (1995) Palladium-catalyzed cross-coupling reactions of organoboron compounds.Chem. Rev.,95, 2457–2483.

[28]. Beletskaya, I.P. and Cheprakov, A.V. (2000) The Heck reaction as a sharpening stone of palladium catalysis.Chem. Rev.,100,3009–3066.

[29]. Corbet, J.-P. and Mignani, G. (2006) Selected patented cross-coupling reactiontechnologies.Chem. Rev.,106,2651–2710.

[30]. Carsten, B., He, F., Son, H.J., Xu, T., and Yu, L. (2011) Stille polycondensation for synthesis of functional materials.Chem. Rev.,111, 1493–1528.

[31] Panagiota Koralli ab, Alkmini D. Nega a, Lida Evmorfia Vagiaki b, Aristea Pavlou bc, Michael G. Siskos c, Antonia Dimitrakopoulou-Strauss a, Vasilis G. Gregoriou ORCID logod and Christos L. Chochos. (2020) New conjugated polymer nanoparticles with high photoluminescence quantum yields for far-red and near infrared fluorescence bioimaging. Mater. Chem. Front, 4, 2357-2369 DOI: 10.1039/D0QM00195C

[32]. Tuncel, D., & Demir, H. V. (2010). Conjugated polymer nanoparticles. Nanoscale, 2(4), 484. doi:10.1039/b9nr00374f

[33] Li, J., Rao, J., & Pu, K. (2018). Recent progress on semiconducting polymer nanoparticles for molecular imaging and cancer phototherapy. Biomaterials, 155, 217–235. doi:10.1016/j.biomaterials.2017.11.025

[34] Y. Wang, P. Li, T. T.-D. Tran, J. Zhang and L. Kong, Manufacturing Techniques and Surface Engineering of Polymer Based Nanoparticles for Targeted Drug Delivery to Cancer, *Nanomaterials*, 2016, 6, 26

[35] Hitoshi Kasai, Hirokazu Kamatani, Shuji Okada, Hidetoshi Oikawa, Hiro Matsuda[1] and Hachiro Nakanishi. (1996). Size-Dependent Colors and Luminescences of Organic Microcrystals. *Jpn. J. Appl. Phys.* 35 L221, https://doi.org/10.1143/JJAP.35.L221

[36]. Haken, J. K. (1992). Modern methods of polymer characterization. Journal of Chromatography A, 606(2), 297–298. doi:10.1016/0021-9673(92)87042-7

[37] P. A. Hassan, S. Rana and G. Verma, Making sense of Brownian motion: Colloid characterization by dynamic light scattering, *Langmuir*, 2015, 31, 12

[38] ISO 22412:2017. Particle Size Analysis–Dynamic Light Scattering (DLS). International Organization for Standardization.

[39] Binder, W. H., & Sachsenhofer, R. (2007). "Click" Chemistry in Polymer and Materials Science. Macromolecular Rapid Communications, 28(1), 15–54. doi:10.1002/marc.200600625

[40]. H.-H. Perkampus, UV-VIS Spectroscopy and Its Applications, DOI: 10.1007/978-3-64277479-9, Chapter 1-3.

[41] S. Roquet, A. Cravino, P. Leriche, O. Alévêque, P. Frère and J. Roncali, Triphenylamine–Thienylenevinylene Hybrid Systems with Internal Charge Transfer as Donor Materials for Heterojunction Solar Cells, *J. Am.*

[42]. Justin Thomas, K. R., Lin, J. T., Velusamy, M., Tao, Y.-T., & Chuen, C.-H. (2004). Color Tuning in Benzo[1,2,5]thiadiazole-Based Small Molecules by Amino Conjugation/Deconjugation: Bright Red-Light-Emitting Diodes. Advanced Functional Materials, 14(1), 83–90. doi:10.1002/adfm.200304486.

[43].H. Raveendranatha Reddya, S. Jayakumarb, R.Subashini, The synthesis and Photophysical studies of Quinoxaline derivatives-Synthesis of Quinoxalines as Cu (II) and Pb (II) ion fluorescent sensors, IJFST (2015), Volume3, p;129-135.

[44] C. V. Rohatgi, T. Harada, E. F. Need, M. Krasowska, D. A. Beattie, G. D. Dickenson, T. A. Smithand and T. W. Kee, Low-Bandgap Conjugated Polymer Dots for Near-Infrared Fluorescence Imaging, ACS Appl. Nano Mater., 2018, 1, 4801 CrossRef CAS.

[45] S. N. Clafton, D. A. Beattie, A. Mierczynska-Vasilev, R. G. Acres, A. C. Morgan and T. W. Kee, Chemical defects in the highly fluorescent conjugated polymer dots, Langmuir, 2010, 26, 17785

[46]. Blanco, E., Shen, H., & Ferrari, M. (2015). Principles of nanoparticle design for overcoming biological barriers to drug delivery. Nature Biotechnology, 33(9), 941–951. doi:10.1038/nbt.3330

[47] William C. Vogt, Congxian Jia, Keith A. Wear, Brian S. Garra M.D., T. Joshua Pfefer (2017). Phantom-based image quality test methods for photoacoustic imaging systems. J. of Biomedical Optics, 22(9), 095002 https://doi.org/10.1117/1.JBO.22.9.095002